

# Qubit-parity interference despite unknown interaction phases

Kratveer Singh,<sup>\*</sup> Kimin Park,<sup>†</sup> Vojtěch Švarc, Artem Kovalenko,  
Tuan Pham, Ondřej Číp, Lukáš Slodička,<sup>‡</sup> and Radim Filip<sup>§</sup>  
*Department of Optics, Palacky University, 77146 Olomouc, Czech Republic*  
(Dated: January 27, 2026)

Quantum interference between interacting systems is fundamental to basic science and quantum technology, but it typically requires precise control of the interaction phases of lasers or microwave generators. Can interference be observed if those interaction phases are stable but unknown, usually prohibitive for complex state without active control? Here, we answer this question by experimentally preparing a Schrödinger-cat-like state of an internal qubit and a motional oscillator of a trapped  $^{40}\text{Ca}^+$  ion, and its robustness to such uncontrolled phases. By applying alternating red and blue sideband pulses, we enforce a strict qubit-parity correlation and interference inherently insensitive to stable but unknown phases of the driving laser. For this qubit-parity interference, we use a minimal two-pulse interferometric sequence to demonstrate characteristic visibilities of 20% and 40%, which approach the theoretical visibility limit, providing a scalable coherence witness without full state tomography for high-dimensional states.

Quantum interference between interacting systems is fundamental to quantum technology. Open systems naturally suffer from decoherence, which limits quantum interference [1]. For nearly closed systems approaching unitary dynamics and initial states close to pure, the interference effect can be exquisitely sensitive to control imperfections. In many systems, such control is provided by a laser (or microwave field) through its phase. The nature of the laser phase itself has been thoroughly studied [2–6]. If such a phase fluctuates rapidly, this acts as stochastic noise, quickly destroying coherence and resulting in a fully mixed state. However, does limited knowledge of a stable phase preclude complex quantum interference experiments?

A particularly challenging quantum scenario involves interference between a low-dimensional system (a qubit) and a high-dimensional one (an oscillator), forming states analogous to Schrödinger’s cat [7–9]. While such states have been demonstrated across various platforms [10–14] and are crucial for sensing and bosonic quantum error correction, where information is stored in the parity of the oscillator [15–20], their creation can be extremely sensitive to interaction phase [21], relying on complex active feedback or precise phase stabilization [21–23]. A primary obstacle is precisely knowing and controlling the phases of the interactions that are linked to the laser phase. If the interaction phase is random between runs, averaging measurements mixes constructive and destructive interference, precluding cat state observation. In many realistic situations, such a laser phase can be stable (non-stochastic) during an experimental run over the timescale of a single experimental sequence ( $\mu\text{s}$ ) but not perfectly known or controlled between sequences.

In this work, we address such a situation by experimentally generating a quantum interference between a trapped-ion qubit and its motion using a preparation sequence of alternating blue and red sideband pulses on a trapped-ion’s oscillator. This sequence deterministically enforces a *qubit energy and oscillator number-parity correlation and their interference*. This qubit-parity structure aligns with cat codes [24–26] and general binomial quantum error correction codes [27], facilitating logical parity manifold preparation. Crucially, while a stable but unknown phase in the laser drive can alter the specific amplitudes *within* the oscillator state, the underlying qubit-parity correlation and interference remains locked by the symmetry of the sideband interactions. To characterize this qubit-parity interference, we measure two minimal visibilities: internal oscillator coherence and mutual qubit-oscillator interference. This structural invariance allows us to achieve 40% visibility in internal oscillator interference and 20% visibility in the qubit-oscillator interference with an increasing mean phonon number, up to  $\langle \hat{n} \rangle \approx 4$ , with standard deviation  $\Delta \hat{n} \approx 4$ , reproducing the theoretical prediction in a scalable way.

For this demonstration, we use a single  $^{40}\text{Ca}^+$  ion in a linear Paul trap. The qubit is encoded in the long-lived ground and excited Zeeman sublevels, and the oscillator is a motional mode of the ion. The optical controls we employ induce elementary Jaynes-Cummings (JC) and anti-JC interactions [28], which controllably entangle the qubit and motional states with an unknown but stable (repeatable)

<sup>\*</sup> These authors contributed equally.; [kratveer.singh@upol.cz](mailto:kratveer.singh@upol.cz); [kratveer050@gmail.com](mailto:kratveer050@gmail.com)

<sup>†</sup> These authors contributed equally.; [park@optics.upol.cz](mailto:park@optics.upol.cz)

<sup>‡</sup> [slodicka@optics.upol.cz](mailto:slodicka@optics.upol.cz)

<sup>§</sup> [filip@optics.upol.cz](mailto:filip@optics.upol.cz)

phase. This method is technically similar to the schemes that employ specific sideband structures for complex state generation [29, 30], and builds upon deterministic, measurement-free preparation of logical states [31]. To analyze the interference, we employ a two-stage verification process: a single-pulse scan first confirms the presence of basic quantum interference between qubit and oscillator, but is insensitive to internal oscillator coherence. Subsequently, a two-pulse sequence with two controllable relative phases minimally but unambiguously resolves the distinct contributions from both qubit-oscillator and internal oscillator coherence. Our study complements a recent experiment on ‘hot’ cat states [32]. While those experiments demonstrate that quantum coherence can be generated *from* an imperfect, thermal initial state, we address a complementary concept: generating and verifying qubit-oscillator interference despite imperfect, uncontrolled interaction dynamics.

We consider the generation of a balanced, qubit-oscillator superposition state of the form, depicted in Fig. 1a.

$$|\Psi\rangle_{\varphi} = 2^{-1/2} (|e\rangle|\psi_{\text{odd}}(\varphi)\rangle + |g\rangle|\psi_{\text{even}}(\varphi)\rangle). \quad (1)$$

Here,  $|g\rangle$  and  $|e\rangle$  are the qubit energy eigenstates. The vector of  $N$  preparation parameters is defined as  $\varphi = (\varphi_1, \varphi_2, \dots, \varphi_N) \in \mathbb{R}^N$ . Each  $\varphi_j \in [0, 2\pi)$  is a static offset that remains constant throughout a single experimental sequence but varies between realizations of such sequences, effectively behaving as a systematic parameter rather than stochastic noise. In such a state,  $|\psi_{\text{odd}}(\varphi)\rangle = \sum_{n=\text{odd}} c_n(\varphi)|n\rangle$  and  $|\psi_{\text{even}}(\varphi)\rangle = \sum_{n=\text{even}} c_n(\varphi)|n\rangle$  with  $c_n \in \mathbb{C}$  are orthogonal motional eigenstates with opposite parity,  $\langle(-1)^{\hat{n}}\rangle = \pm 1$ , respectively. Here,  $|n\rangle$  is an oscillator Fock state. This state  $|\Psi\rangle_{\varphi}$  in (1) is characterized minimally by two distinct phase-sensitive effects. First, the state possesses *mutual qubit-parity interference*, representing a stable phase relationship between the qubit state and the oscillator’s parity. This coherence leads to interference effects that can be controlled by the relative phase  $\theta$ :

$$|\Psi\rangle_{\theta} = 2^{-1/2} (e^{i\theta}|e\rangle|\psi_{\text{odd}}(\varphi)\rangle + |g\rangle|\psi_{\text{even}}(\varphi)\rangle). \quad (2)$$

Here, phase  $\theta$  can be controlled by a local qubit phase rotation by a unitary operator  $e^{i\theta\hat{\sigma}_z/2}$ , up to a global phase.

Second, the motional states  $|\psi_{\text{odd/even}}(\varphi)\rangle$  themselves possess *internal oscillator coherence*, a stable phase relationship among their constituent Fock states. This coherence can be analogously probed by applying a local oscillator phase  $\Theta$ . This is described by a motional phase rotation, where the operator  $\exp[i\Theta\hat{n}]$  applies a phase  $e^{i\Theta n}$  to each Fock state component  $|n\rangle$ . The complete state, including both types of phase-sensitive effects, is then given by:

$$|\Psi\rangle_{\theta, \Theta} = \exp[i\Theta\hat{n}]|\Psi\rangle_{\theta} = 2^{-1/2} (e^{i\theta}|e\rangle|\psi_{\text{odd}}(\varphi, \Theta)\rangle + |g\rangle|\psi_{\text{even}}(\varphi, \Theta)\rangle), \quad (3)$$

where the motional states are defined as  $|\psi_{\text{odd/even}}(\varphi, \Theta)\rangle \equiv \exp[i\Theta\hat{n}]|\psi_{\text{odd/even}}(\varphi)\rangle$ .

A two-pulse measurement sequence provides an orthogonal mapping of the qubit-oscillator and internal oscillator coherences, characterizing their respective contributions to the observed interference, thus validates the state structure. The core principle of robust qubit-oscillator interference and internal oscillator coherence is this qubit-parity correlation in the superposition state  $|\Psi\rangle_{\theta, \Theta}$ , preserving the orthogonality of the motional parity subspaces regardless of the values in  $\varphi$ .

The phase  $\theta$  is the relative phase between the two components of the superposition in Eq. (1). It represents the coherence between the qubit being in  $|g\rangle$  with an even-parity motion and in  $|e\rangle$  with an odd-parity motion. Instability in  $\theta$  between runs destroys this coherence, reducing the system to a mixed state described by qubit dephasing:

$$\rho_{\text{Q-dep}} = \frac{1}{2} |e\rangle\langle e| \otimes |\psi_{-}\rangle\langle\psi_{-}| + \frac{1}{2} |g\rangle\langle g| \otimes |\psi_{+}\rangle\langle\psi_{+}|. \quad (4)$$

Here, the motional states  $|\psi_{\pm}\rangle$  retain their internal coherence but are only classically correlated with the qubit state. If strong motional dephasing also occurs, or if all the preparation pulses are unstable, this motional coherence is also lost, resulting in a state fully diagonal in the qubit-Fock basis:

$$\rho_{\text{O-dep}} = \frac{1}{2} |e\rangle\langle e| \otimes \text{diag}[|\psi_{-}\rangle\langle\psi_{-}|] + \frac{1}{2} |g\rangle\langle g| \otimes \text{diag}[|\psi_{+}\rangle\langle\psi_{+}|]. \quad (5)$$

Our experiment aims to demonstrate both qubit-oscillator interference and internal oscillator coherence despite stable but unknown phases of the preparation pulses, distinguishing the pure state  $|\Psi\rangle$  from these incoherent mixtures ( $\rho_{\text{Q-dep}}$ ,  $\rho_{\text{O-dep}}$ ), as detailed in Appendix D.

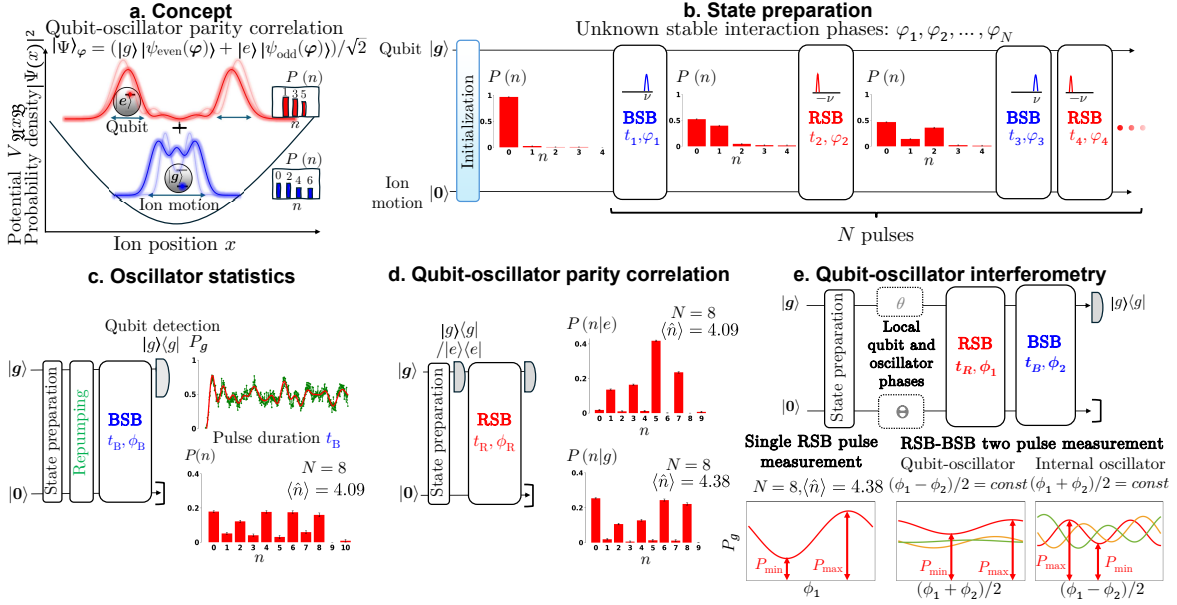


Figure 1. **Creating and verifying qubit-oscillator interference and internal oscillator coherence in a trapped ion despite unknown interaction phases.** **a** Visualization of the qubit-parity correlation in the state  $|\Psi\rangle_\varphi$  (1), where the qubit state dictates the parity of the motional state. **b** The state preparation sequence, consisting of alternating blue- and red-sideband (BSB, RSB) pulses producing Jaynes-Cummings and anti-Jaynes-Cummings interactions with stable but unknown interaction phases  $\varphi_i$ . **c** The measured phonon number distribution  $P(n)$  obtained via Rabi flopping (described in Appendix J), showing a significant mean phonon number ( $\langle \hat{n} \rangle = 4.09$ ) and standard deviation. The BSB pulse duration  $t_B$  is varied, while the pulse phase  $\phi_B$  is fixed. **d** Measurement of the qubit-parity correlation, confirming that the ground (excited) qubit state is associated with even (odd) phonon numbers (Figure 2c,d). The RSB pulse duration  $t_R$  is varied, while the pulse phase  $\phi_R$  is fixed. **e** A two-pulse verification sequence with experimentally scanned phases  $\phi_1$  and  $\phi_2$  used to measure interference fringes in the final qubit ground state population  $P_g$ , from the state in **c** and **d** ( $N = 8$ ,  $\langle \hat{n} \rangle \approx 4$ ). Solid lines represent fits to experimental data; different colors indicate distinct phase constraints. Without full state tomography and active control of local phases  $\theta$  and  $\Theta$ , this measurement directly distinguishes between the two fundamental types of coherence: *Qubit-oscillator interference* (locally controllable by the qubit phase  $\theta$ ) represents the coherence between the qubit’s state and the motion’s parity. The lowest order qubit-oscillator interference can be sufficiently measured using a single red pulse measurement. Its higher order interference is probed by scanning the phase sum of the two verification pulses,  $\frac{\phi_1 + \phi_2}{2}$  while the phase difference  $\frac{\phi_1 - \phi_2}{2}$  is constrained by different values. *Internal oscillator coherence* (locally controllable by the oscillator phase  $\Theta$ ) representing coherence between different motional components within a single parity subspace, is probed by scanning the phase difference  $\frac{\phi_1 - \phi_2}{2}$ , while the phase sum is held constant by different values. The contrast and visibility of all these curves are averaged over the phases  $\varphi_i$  for  $i = 1, \dots, N$ .

**Preparation** We describe the states in the qubit-Fock basis  $|g(e), n\rangle$ . We begin with the qubit-oscillator ground state  $|g, 0\rangle$  achieved by cooling, and apply a sequence of alternating blue sideband (BSB) and red sideband (RSB) pulses for preparation depicted in Fig. 1b, which are defined with details in Appendix C. BSB (RSB) pulses increase the maximum motional quantum number while exciting (de-exciting) the qubit, as well as the standard deviation of the Fock distribution for a broad range of pulse areas. Together, these alternating pulses coherently drive the system to the desired qubit-motional state. The total  $N$  pulse sequence is described by the unitary operator  $\hat{U}_{\text{prep}}$ , a sequential product of  $N$  anti-Jaynes-Cummings (BSB,  $\hat{U}_{\text{aJC}}$ ) and Jaynes-Cummings (RSB,  $\hat{U}_{\text{JC}}$ ) interactions as in Fig. 1b:

$$\hat{U}_{\text{prep}} = \prod_{j=1}^{N/2} \hat{U}_{\text{JC}}[t_{2j}, \varphi_{2j}] \hat{U}_{\text{aJC}}[t_{2j-1}, \varphi_{2j-1}], \quad (6)$$

where  $\varphi_j$  comprise  $\varphi$  in Eq. (1). For odd  $N$ , the preparation sequence ends with BSB pulse, without the final RSB pulse.

In our experiment, we relax the challenging constraint on small time steps of  $t_j \ll 1$  and perfectly controlled phases of  $\varphi_j$ , typically needed for Suzuki-Trotter decomposition [33]. Our approach instead

accommodates *stable but unknown* phase offsets in the phases of laser driving fields ( $\varphi_j$  in Eq. (6)) inherent to the setup (e.g., corresponding to the stable relative phases within the common laser-qubit coherence and assuming the motional coherence to be much longer) throughout the experiment but are not actively controlled to specific target values. Quantitatively, the phase remains constant over the timescale of a single experimental sequence (on the order of milliseconds), with particular limits on the coherence time detailed in Appendix J. These stable but unknown phases have a crucial distinction from stochastic, shot-to-shot noise of these interaction phases  $\varphi_j$ , to which this method is not immune [34].

The first preparation pulse acts on the initial state  $|g, 0\rangle$ , where the qubit is in ground state  $|g\rangle$  and the motional state has an *even* phonon number ( $n = 0$ ). The second pulse already acts on the qubit-oscillator correlation. Following Fig. 1b we apply:

1. **First (BSB) pulse:** A blue-sideband pulse can only transition the system to  $|e, 1\rangle$  as  $|\Psi_1\rangle = \cos(t_1)|g, 0\rangle + e^{i\varphi_1}\sin(t_1)|e, 1\rangle$ . The qubit state  $|e\rangle$  is now linked exclusively to an *odd* phonon number ( $n = 1$ ).
2. **Second (RSB) pulse:** A subsequent red-sideband pulse can only act on the new  $|e, 1\rangle$  component, transitioning it back to  $|g, 2\rangle$  as  $|\Psi_2\rangle = \cos(t_1)|g, 0\rangle + e^{i\varphi_1}\sin(t_1)\cos(t_2)|e, 1\rangle + e^{i(\varphi_1+\varphi_2)}\sin(t_1)\sin(t_2)|g, 2\rangle$ . The qubit state  $|g\rangle$  is thus again linked only to an *even* phonon number.

This alternating sequence, that can be extended further, enforces the qubit-parity correlation throughout the circuit. The phases  $\varphi_j$  modulate transition amplitudes but leave the qubit-parity structure invariant.

The alternating sideband pulses described in Fig. 1b enforce a strict qubit-parity correlation—linking the qubit state  $|g\rangle$  to even phonon numbers  $n$  and  $|e\rangle$  to odd  $n$ —which ensures the generation of the target state structure (Eq. (1)) regardless of the phases  $\varphi$ . While this fundamental structure is preserved, the specific complex coefficients  $c_n(\varphi)$  and the overall relative phase  $\theta$  depend on the preparation phases and pulse lengths. To simplify the experimental demonstration, the target pulse area for each step in our experiment is set to  $\eta\Omega_0 t_j \approx \pi/4$  (i.e.  $\pi/2$  pulse), which corresponds to a half-transfer of population for the  $n = 0 \leftrightarrow n = 1$  transition.

Following the state preparation sequence, we characterize the resulting state and verify its fundamental structure. First, we measure the phonon number distribution  $P(n)$ , confirming the creation of a macroscopic motional state with a significant mean phonon number, as conceptually depicted in Fig. 1c. Subsequently, we verify the state’s key structural feature by measuring the qubit-parity correlation (Fig. 1d). This confirms that the qubit ground state  $|g\rangle$  is exclusively associated with even phonon numbers, while the excited state  $|e\rangle$  is associated with odd phonon numbers, a correlation central to our experimental robustness. The details of these experiments are summarized in Appendix J.

**Interference by single-pulse measurement** Our first step is to distinguish the prepared state  $|\Psi\rangle$  from a fully incoherent mixed state, such as  $\rho_{O\text{-dep}}$  (Eq. (5)). We apply a single RSB verification pulse with a variable phase  $\phi_1$ , which drives transitions like  $|g, 2n\rangle \leftrightarrow |e, 2n - 1\rangle$ . Scanning the phase  $\phi_1$  of this single verification pulse directly creates and reveals interference between the  $|g\rangle|\psi_{\text{even}}(\varphi)\rangle$  and  $|e\rangle|\psi_{\text{odd}}(\varphi)\rangle$  components of the state (1). If the state possesses qubit-oscillator coherence in subspaces  $\{|g, 2n\rangle, |e, 2n - 1\rangle\}$  for any integer  $n$ , the final qubit population  $P_g$  will modulate as a sinusoidal function of  $\phi_1$  (Fig. 1e, left). While this confirms some interference, it cannot resolve internal oscillator or coherence, necessitating a longer sequence. The prepared state may still have only qubit-oscillator coherence, in the density matrix of  $\rho = \sum_n |\psi_n\rangle\langle\psi_n|$ , where  $|\psi_n\rangle = c_{2n}|g, 2n\rangle + c_{2n-1}|e, 2n - 1\rangle$  with complex coefficients  $c_j$  compatible with the observed qubit-oscillator parity correlation. Therefore, the single-pulse measurement acts as a crucial witness of coherence, confirming the prepared state is not a simple incoherent mixture such as  $\rho_{Q\text{-dep}}$  (4) or  $\rho_{O\text{-dep}}$  (5), while it cannot on its own unambiguously resolve them. To systematically characterize the higher-order coherence contributions probed in our measurements, throughout the work, we define the  $k$ -th order off-diagonal Fock elements as  $|\langle n|\rho_O|n - k\rangle|$  for any integer  $n$  with  $0 \leq k \leq n$ , where  $\rho_O$  is the reduced density matrix of the oscillator. Due to the choice of verification pulse length  $t_R = \pi/2$ , the dominant term contributing to the contrast and visibility here is from  $\langle 2|\rho_O|1\rangle$ , which belongs to the 1st order off-diagonal.

**Interference by two-pulse measurement** We next apply a two-pulse verification sequence consisting of a RSB pulse with phase  $\phi_1$  followed by a BSB pulse with phase  $\phi_2$ , as in Figure 1e. This

method maps the experimental verification phases  $\phi_1$  and  $\phi_2$  to the local phases  $\theta$  and  $\Theta$  (Eq. 3). This relationship is a direct consequence of the measurement interaction, as we derive from the operator commutation relations in Appendix E. The two verification pulses project the prepared state onto a measurement basis of the form

$$|\Psi_m(\phi_1, \phi_2)\rangle = 2^{-1/2} \left( |e\rangle |\psi_{\text{odd}}^{(\text{measure})}(\phi_1, \phi_2)\rangle + |g\rangle |\psi_{\text{even}}^{(\text{measure})}(\phi_1, \phi_2)\rangle \right), \quad (7)$$

where  $|\psi_{\text{odd}}^{(\text{measure})}(\phi_1, \phi_2)\rangle$  and  $|\psi_{\text{even}}^{(\text{measure})}(\phi_1, \phi_2)\rangle$  are also distinct, orthogonal motional states of the oscillator that possess opposite parity, but may have different (here typically smaller) average number of quanta than  $|\psi_{\text{odd}}(\varphi)\rangle$  and  $|\psi_{\text{even}}(\varphi)\rangle$ . We then measure the final ground state population,

$$P_g = |\langle \Psi_m(\phi_1, \phi_2) | \Psi \rangle_{\varphi}|^2 = \frac{1}{4} |\langle \psi_{\text{even}}^{(\text{measure})} | \psi_{\text{even}}(\Theta) \rangle + e^{i\theta} \langle \psi_{\text{odd}}^{(\text{measure})} | \psi_{\text{odd}}(\Theta) \rangle|^2, \quad (8)$$

that oscillates as a function of the phases  $\phi_{1,2}$ . Due to the choice of verification pulse length  $t_R = \pi/2$ , the dominant term contributing to the contrast by this measurement is from  $\langle 2 | \rho_O | 1 \rangle$  and  $\langle 4 | \rho_O | 1 \rangle$ .

Specifically, as proven by the unitary transformations in Eqs. (E1–E4), the final qubit population  $P_g$  depends functionally on the terms  $\theta - \frac{\phi_1 + \phi_2}{2}$  (qubit-oscillator interference) and  $\Theta - \frac{\phi_1 - \phi_2}{2}$  (internal oscillator coherence), and thus scanning the phase sum  $(\phi_1 + \phi_2)/2$  has the identical effect on the modulation by the qubit-oscillator coherence  $\theta$  for fixed phase difference  $(\phi_1 - \phi_2)/2$ , while scanning the phase difference  $(\phi_1 - \phi_2)/2$  has the identical modulation by the internal oscillator coherence  $\Theta$  for fixed phase sum  $(\phi_1 + \phi_2)/2$ . This establishes a direct orthogonal mapping between our experimental control parameters and the two distinct coherences we aim to independently probe. Figure 1e conceptually represents this mapping with perpendicular  $\theta$  and  $\Theta$  axes.

Beyond these independent projections, the full two-dimensional interference landscape captures the state's next order qubit-parity coherence and interference, upto  $|g, 2n\rangle \leftrightarrow |e, 2n \pm 3\rangle$ . As detailed in Appendix G, our two-pulse sequence is sensitive to coherence terms  $|n\rangle\langle m|$  between Fock states of the same parity up to a separation of  $|n - m| \leq 3$ . This sequence extends the single pulse verification by probing this third-order Fock coherences. This range of Fock separation is sufficient for our purpose, which is to verify the creation of a non-classical state by measuring its quantum signatures. For instance, the two-pulse sequence is capable of probing third-order coherence terms, such as  $|g, n\rangle\langle e, n - 3|$ , which are a blind spot for the single-pulse method.

*Internal oscillator coherence*, the phase relationship *within* a single parity subspace, probed by scanning the phase difference,  $(\phi_1 - \phi_2)/2$ , tests interference *among the different Fock state components* (e.g. between  $|g, n\rangle$  and  $|g, n + 2\rangle$ ) within a single parity subspace, establishing a signature of parity definiteness with multi-phonon components in the motional state. This makes the phase difference a probe for specific orders of internal oscillator coherence  $\Theta$ .

Any experimental state is subject to decoherence, which makes long-range coherences profoundly more fragile than short-range ones. To quantitatively distinguish our prepared state from an incoherent mixture as detailed in Appendix D, we consider a phenomenological model: if the coherence between adjacent number states  $|n\rangle\langle n - 1|$  is described by a factor  $w \leq 1$ , the coherence for a separation of  $k = |n - m|$  would scale as  $w^k$ , decaying exponentially. In the prepared states, the long range coherence  $|n - m| > 3$  would be present if  $1 - w \ll 1$ . While the current two pulse verification scheme is blind to them, it can be used to estimate  $w$ . Our two-pulse sequence is therefore a sufficient probe for the short range coherences ( $k \leq 3$ ), which may be used to infer the long range coherence factors that would survive if  $w \approx 1$ . Furthermore, as detailed in Appendix E, the total contrast measured over the full  $(\phi_1, \phi_2)$  space roughly corresponds to the weighted sum of both qubit-oscillator and internal oscillator coherence magnitudes.

**Interference quantification.** We quantify both interferences by the single-pulse and two-pulse measurements using two standard metrics. The contrast  $C(\varphi) \equiv P_{\text{max}}(\varphi) - P_{\text{min}}(\varphi)$  measures the absolute amplitude of the population oscillation, where  $P_{\text{max}}(\varphi)$  and  $P_{\text{min}}(\varphi)$  are the maximal and minimal values of a measured probability distribution  $P_g$  from the state and measurement over  $\theta$  and  $\Theta$ , or equivalently over  $\phi = (\phi_1, \phi_2)$ . It is sensitive to both the underlying coherence and the overlap between the prepared state and the measurement basis. Low contrast can result from either decoherence or a non-optimal measurement setting, even for a pure state. The normalized contrast, or visibility  $V(\varphi) \equiv (P_{\text{max}}(\varphi) - P_{\text{min}}(\varphi)) / (P_{\text{max}}(\varphi) + P_{\text{min}}(\varphi))$  is fundamentally a measure of the clarity of the interference fringe. Crucially, high visibility normalizes against *global population loss* provided the interfering pathways remain balanced; however, it remains strictly bounded by the state's *internal coherence*, as stochastic dephasing eventually fills the interference

minima and suppresses visibility. Therefore, visibility serves as our primary quantifier of coherence. Its upper bound is constrained by the *spectral mismatch*—the imperfect overlap between the prepared state’s Fock-state distribution and the states projected by the verification pulses [28, 35]. This mismatch in number-state support limits the maximum achievable visibility even for ideal pure states. To illustrate, consider an interference experiment where a prepared state with motional components  $|\psi_{\text{odd}}(\varphi)\rangle$  and  $|\psi_{\text{even}}(\varphi)\rangle$  in (1) is projected onto a measurement basis with components  $|\psi_{\text{odd}}^{(\text{measure})}(\phi)\rangle$  and  $|\psi_{\text{even}}^{(\text{measure})}(\phi)\rangle$  in (7). The contrast and visibility, for the prepared balanced states, are determined by the overlap between the prepared state  $|\Psi\rangle_{\theta,\Theta}$  in Eq. (3) and the measurement basis  $|\Psi_m\rangle$  in Eq. (7). Defining the overlaps of even and odd components as  $\alpha_e(\varphi) = \langle\psi_{\text{even}}^{(\text{measure})}(\phi_1, \phi_2)|\psi_{\text{even}}(\varphi, \Theta)\rangle$  and  $\alpha_o(\varphi) = \langle\psi_{\text{odd}}^{(\text{measure})}(\phi_1, \phi_2)|\psi_{\text{odd}}(\varphi, \Theta)\rangle$ , the contrast and visibility about  $\theta$  are  $C(\varphi) = |\alpha_e(\varphi)\alpha_o^*(\varphi)|$  and  $V(\varphi) = 2|\alpha_e(\varphi)\alpha_o^*(\varphi)|/(|\alpha_e(\varphi)|^2 + |\alpha_o(\varphi)|^2)$ . The visibility is maximized when the magnitudes of the interfering pathway overlaps are balanced:  $\left|\langle\psi_{\text{even}}^{(\text{measure})}(\phi)|\psi_{\text{odd}}(\varphi)\rangle\right| = \left|\langle\psi_{\text{odd}}^{(\text{measure})}(\phi)|\psi_{\text{even}}(\varphi)\rangle\right|$ . High visibility (approaching 1), which indicates such balanced interfering pathways, allows for a perfectly dark output (zero population) at the interference minimum in a qubit-oscillator interference. In order to account for interaction parameters, we average the contrast and visibility over many realizations of the interaction phases  $\varphi$  during the state preparation, throughout the work as

$$\langle C \rangle = \frac{1}{(2\pi)^N} \int_{\varphi} d\varphi C(\varphi), \quad \langle V \rangle = \frac{1}{(2\pi)^N} \int_{\varphi} d\varphi V(\varphi), \quad (9)$$

where the integration is over all possible parameters in  $\varphi$ . We computed the integral numerically using a Monte Carlo method, for which the averages saturate rapidly with the number of samples, and experimentally over larger than 100 realizations.

## RESULTS

**Measurement of Oscillator Statistics** Rabi flopping (Fig. 1c) reveals motional excitation increasing with  $N$ , saturating at  $\langle \hat{n} \rangle \approx \Delta \hat{n} \approx 4$ . The ratio  $\langle \hat{n} \rangle / \Delta \hat{n} \approx 1$  arises from the fixed-duration pulse choice (Fig. 2a), validating the deterministic generation of complex motional states.

Figure 2a shows the average phonon number  $\langle \hat{n} \rangle$ , its standard deviation  $\Delta \hat{n}$  and their saturation to a value of approximately 4 at large  $N$ , a consequence of the fixed pulse length. As shown by the simulation in Fig. 2a, dynamically adjusting the pulse durations to account for the  $\sqrt{n}$ -dependence of the Rabi frequency would allow for continued growth of the motional state size. Since the sideband Rabi frequency depends on the phonon number  $n$ , our fixed-duration pulse eventually acts as a  $2\pi$  pulse for a specific high- $n$  transition. This completes a full Rabi cycle, preventing further population transfer and capping the motional excitation. This saturation is an experimental byproduct of fixed-area pulses rather than a fundamental limitation of the protocol’s scalability, and a larger motional states can be generated simply by adjusting the pulse duration.

A core feature of our experiment is the deterministic generation of a state with a strong qubit-parity correlation. Crucially, we verify the foundational qubit-parity correlation. As shown conceptually in Fig. 1d, projective measurements together with Rabi flopping confirm the expected parity-qubit association across all preparation steps. While ideal theory predicts a perfect, strict correlation, experimental factors may lead to a small degradation of this structure, as seen in Fig 2c. The results, presented in Figure 2d, confirm the preservation of the parity-qubit lock. The decoherence model detailed in Appendix D indicates that the system maintains a high degree of purity. We confirm that conditioning on the ground state  $|g\rangle$  consistently yields a positive average parity  $\langle (-1)^{\hat{n}} \rangle$ , indicating that the motional state is composed of dominantly even phonon numbers. Conversely, conditioning on the excited state  $|e\rangle$  yields a negative average parity, although its correlation with odd phonon numbers were only weakly manifested for data sets with  $N \leq 6$ . We note that these reported odd-parity values are affected by increased photodetection noise, as the odd components are less populated in the prepared superposition states; this effect becomes more pronounced for smaller  $N$ . In addition, the population measurements are highly sensitive to the durations of the probing Rabi pulses, which further reduces the evaluated parity values. Consequently, the reported results should be regarded as a lower bound on the average parity of the prepared states. This imprinting of the desired structure demonstrates that the alternating sideband pulse sequence works as intended, enforcing the qubit-parity correlation that is robust to the unknown-but-stable interaction phases.

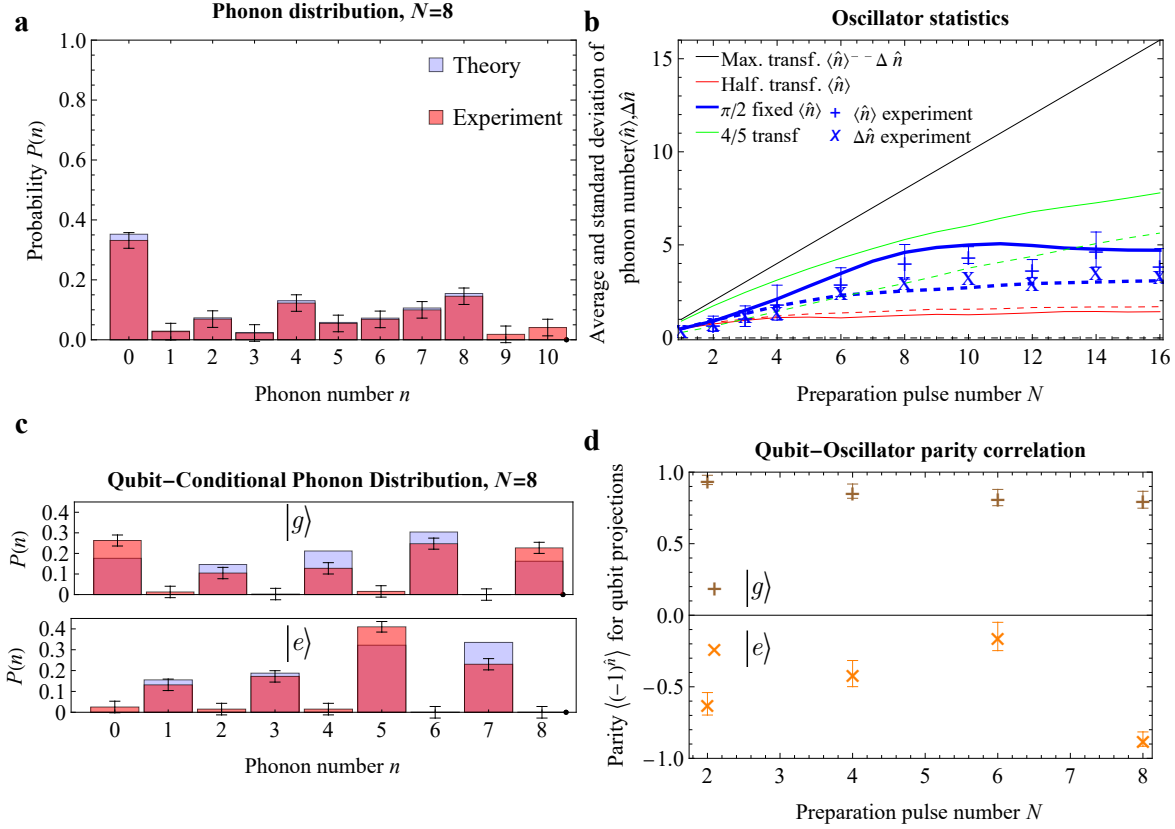


Figure 2. **Oscillator statistics.** **a** Phonon number distribution  $P(n)$  for a state prepared with  $N = 8$  pulses. The plot compares the experimentally measured distribution (red) against the theoretical prediction (light blue, see Appendix A), showing the creation of a dispersed motional state. **b** Growth of the mean phonon number  $\langle \hat{n} \rangle$  and its standard deviation  $\Delta \hat{n}$  with the number of preparation pulses  $N$ . This confirms the generation of increasingly populated and adequately delocalized motional states. **c** Conditional phonon number distributions demonstrating the strong qubit-parity correlation in the dispersed  $P(n)$ . Deviations between experiment and theory are color-coded by sign (orange: positive, light blue: negative). (Top) the distribution when the qubit is measured in the ground state  $|g\rangle$ , which is composed of dominantly even phonon numbers. (Bottom) The distribution for the excited state  $|e\rangle$ , composed of dominantly odd phonon numbers. **d** Measurement of the qubit-parity correlation. The average motional parity  $\langle (-1)^{\hat{n}} \rangle$  as a function of the preparation pulse number,  $N$ . The data confirms that the ground (excited) qubit state is correlated with even (odd) phonon numbers, demonstrating the imprinting of the desired state structure.

**Interference by single- and two-pulse measurements** To validate our experiment, we employ a two-way approach for theoretical comparisons. First, to confirm the accuracy of our underlying physical model, we show that it can precisely reproduce the data from a specific experimental run by treating the unknown-but-stable interaction phases ( $\phi_i$ ) as fitting parameters. Second, to demonstrate the general robustness of our experiment, we compare the experimental metrics against theoretical predictions that have been averaged over all possible (practically randomly sampled) interaction phases. This second method requires no fitting and directly tests the expected average-case performance.

Figure 3 shows the measured contrast of this modulation versus the number of preparation pulses  $N$  obtained from a single-pulse verification scan. The strong interference confirms that coherence is successfully generated and maintained, ruling out a fully mixed state. This contrast directly measures the interference between the qubit and the oscillator's parity subspaces, reflecting their mutual coherence. The plot compares our experimental data (blue crosses) with theoretical predictions for two different pulse strategies: our fixed  $\pi/2$  pulse method (blue squares) and an ideal half-transfer scenario (red triangles). The experimental results follow the general trend of the fixed  $\pi/2$  model, showing a decrease in contrast as the state's complexity (and mean phonon number) grows, before leveling off at a saturated value of  $\sim 0.2$  for  $N \geq 8$ . The observed saturation and the deviation from the ideal

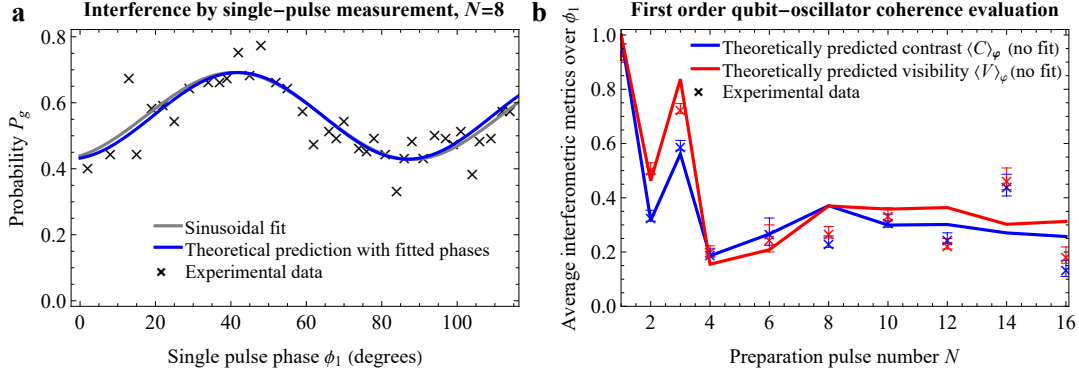


Figure 3. **Interference by single-pulse measurement.** **a** Interference fringe from a single-pulse verification measurement for  $N = 8$ . The final ground state population,  $P_g$ , is plotted as a function of the verification pulse phase,  $\phi_1$ . The theoretical curve represents a fit to this specific dataset, using the unknown preparation phases as parameters to validate the accuracy of our model for a single realization. **b** Contrast and visibility of the final qubit population modulation  $P_g$  from a single-pulse verification scan. The theoretical prediction curves, which require no fitting, are averaged over all possible unknown stable phases to show the expected performance. This non-zero contrast confirms the presence of coherence in the prepared state, distinguishing it from a simple incoherent mixture (4) or (5).

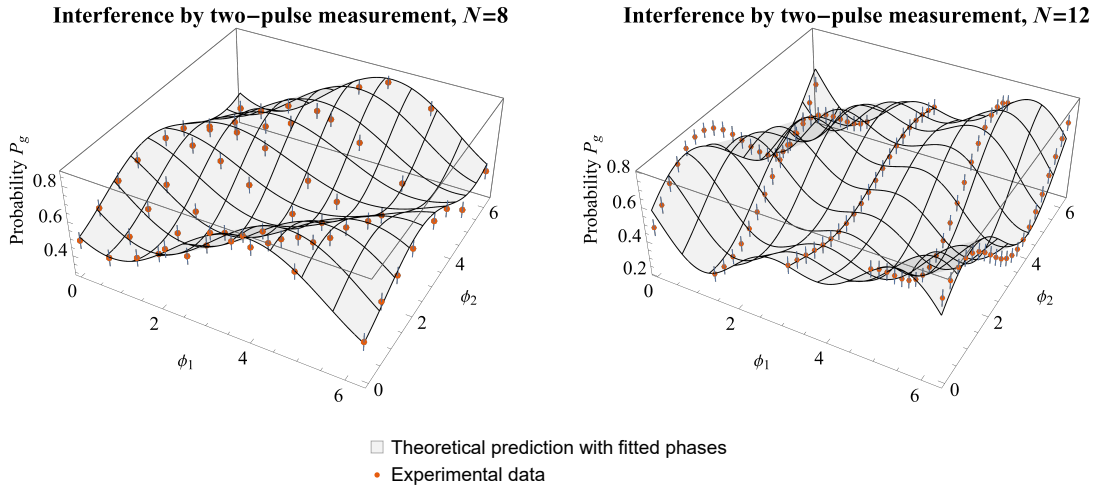


Figure 4. **Two-dimensional interference landscape** for **a**  $N = 8$  and **b**  $N = 12$  pulses. Experimental data (points) are overlaid with a theoretical model where the interaction phases have been fitted to these specific runs. The excellent agreement validates the model's ability to describe individual experimental outcomes.

half-transfer case, particularly at larger  $N$ , can be attributed to a combination of two factors: the specific state and detection properties by our pulse sequence, and the accumulation of decoherence from environmental noise sources during the longer pulse sequences. This general decoherence, distinct from the stable phase error our experiment is designed specifically to resist, reduces the overall coherent fraction of the state, thereby lowering the absolute contrast.

Figure 4 provides a detailed visualization of the two-dimensional interference landscape for a state prepared with  $N = 8$  pulses, which serves as the foundational data for the summary metrics presented in Figure 5. Specifically, Figure 4 shows the experimentally measured ground state probability,  $P_g$ , as a function of the two independent verification phases,  $\phi_1$  and  $\phi_2$ . This two-dimensional data is then projected onto two orthogonal axes to independently analyze the two distinct types of coherence. The projection onto the phase sum axis,  $(\phi_1 + \phi_2)/2$ , isolates the interference fringes that are a direct signature of the *qubit-oscillator coherence* (Figure 5a). Conversely, the projection onto the phase difference axis,  $(\phi_1 - \phi_2)/2$ , isolates the interference fringes that are a direct signature of the *internal oscillator coherence*, depicted in Figure 5c. From each of these one-dimensional interference fringes,

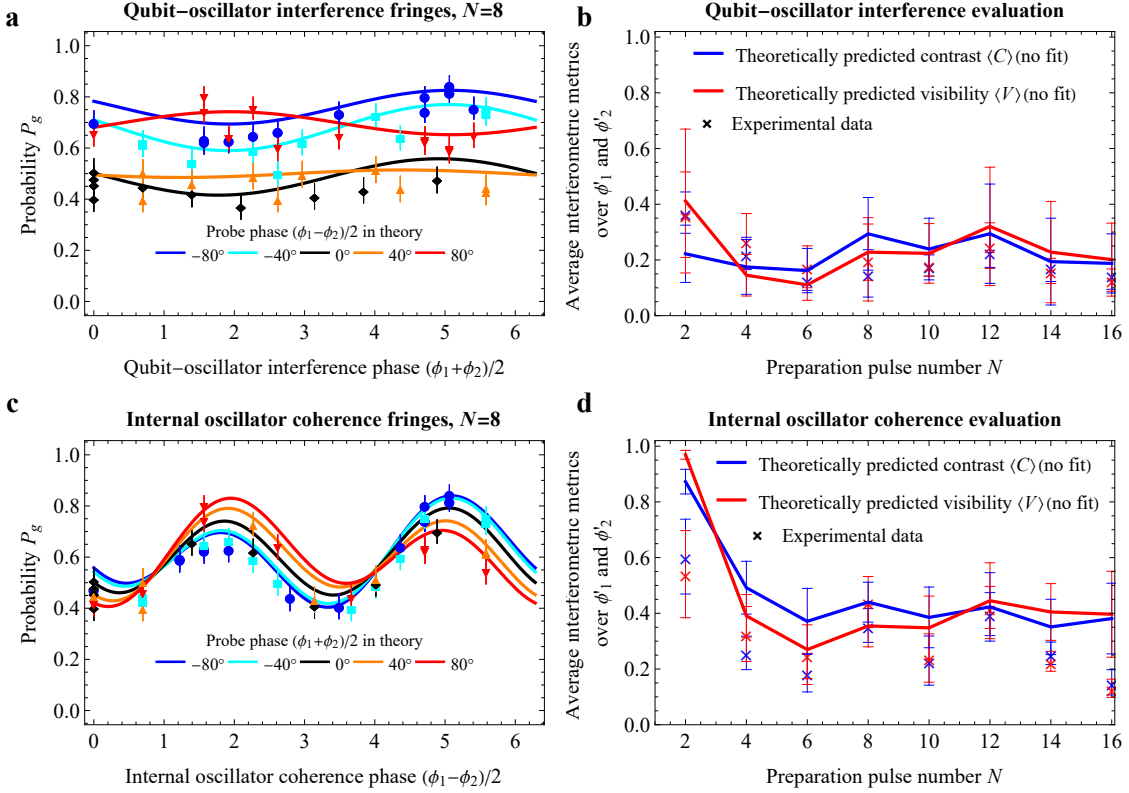


Figure 5. **Interference by two-pulse measurements.** (a, c) Interference fringes for  $N = 8$ , showing agreement between experimental data and our theoretical model when the unknown interaction phases  $\varphi$  are fitted to the specific dataset. (b, d) Average interferometric metrics versus preparation pulse number  $N$ . Experimental data is compared against parameter-free ideal theoretical predictions that have been averaged over randomly sampled all possible interaction phases. The close agreement with the theoretical visibility fundamentally bounded (to the theoretical value  $\lesssim 0.5$ ) validates the general robustness to unknown phases. This effect is present in both the experimental data and the theoretical predictions.

the maximum ( $P_{\max}$ ) and minimum ( $P_{\min}$ ) population values are extracted. These values are then used to compute the two key interferometric metrics, the averaged contrast and the visibility (9).

The results are presented in Figure 5, which plots the average interference contrast  $\langle C \rangle$  and visibility  $\langle V \rangle$  (9) against  $N$ . Figure 5b isolates the qubit-oscillator interference (probed by the phase half sum  $\frac{\phi_1 + \phi_2}{2}$ ), while Figure 5d probes the internal oscillator coherence (probed by the phase half difference  $\frac{\phi_1 - \phi_2}{2}$ ). In both independent measurements, the experimental data for contrast and visibility closely track their respective theoretical predictions without fitting. A crucial aspect of this analysis is the theoretical maximum visibility matching the theoretical limits of  $\approx 0.4$  for internal oscillator interference, while  $\approx 0.2$  for the qubit-oscillator interference, a ceiling imposed by the inherent mismatch between our prepared state and the measurement basis. For the internal oscillator coherence, the dominant contribution to the averaged contrast and visibility comes from the second-order coherence terms  $|\langle n | \rho_O | n - 2 \rangle|$ , where  $\rho_O$  is the reduced density matrix of the oscillator. The excellent agreement across both projections provides unambiguous evidence that the experiment generates and maintains a complex quantum state with both types of coherence. This decay in coherence also saturates for  $N \gtrsim 8$ , matching the theoretical prediction, a behavior interlinked with the saturation of the state's complexity seen in Fig. 2: once the state stops growing, the rate of accumulating decoherence also stabilizes, leading to the observed plateau in the coherence metrics. The observed decay at higher  $N$  deviating from the theory can be attributed to a quantifiable effect of accumulating experimental imperfections. The increased sequence duration for larger  $N$  allows more time for time-dependent decoherence, such as motional heating from electric-field noise and qubit dephasing from magnetic-field fluctuations. Furthermore, each of the  $N$  control pulses contributes a small random error from laser fluctuations, and these errors compound, reducing the final state fidelity. A key feature of the data in Fig. 5 is the near-identical measured average contrast  $\langle C \rangle$  and visibility  $\langle V \rangle$ , especially for a low

number of preparation pulses  $N$ . From their definitions, the condition  $\langle C \rangle \approx \langle V \rangle$  mathematically implies that  $P_{\max} + P_{\min} \approx 1$  for various realizations. This is a direct signature of a well-balanced interferometric measurement, where the two interfering quantum pathways—defined by the projection of the prepared state onto the measurement basis—have nearly equal effective amplitudes. Notably, the experimental visibility remains close to the contrast for both single- and two-pulse measurements as in Figs 3 and 5.

A key feature in Fig. 5 is the higher measured visibility for internal oscillator coherence compared to qubit-oscillator coherence. The theoretical model for a general qubit-oscillator correlated states not bound to any preparation, including qubit-parity correlated states, imposes higher maximum visibilities and contrasts for internal oscillator coherence than those for qubit-oscillator coherence. To quantify the state purity beyond raw visibility, we find the purity about  $\approx 0.82$  ( $w \gtrsim 0.9$ ) as in Appendix D, indicating that the observed contrast is nearly optimal and the system maintains a high degree of underlying quantum coherence despite the spectral mismatch with the measurement basis.

## CONCLUSION

We have proposed and experimentally demonstrated generation and verification of qubit-parity correlation and interference in the presence of stable but unknown phases. The resulting states exhibit a substantial interference visibility and contrast of approximately 0.4 (theoretically  $\approx 0.47$ ) for internal oscillator coherence, and 0.2 (theoretically  $\approx 0.22$ ) for qubit-oscillator interference. Crucially, these values show strong agreement with the theoretical maximum visibility imposed by our measurement method. The close correspondence demonstrates that the primary constraint on visibility is the overlap between our prepared state and measurement basis, rather than infidelity. This ceiling of visibility and contrast can be further enhanced by optimizing the verification pulse area. The two-pulse measurement sequence provides a robust, unambiguous witness of interference from hybrid coherence that avoids potential false-positive visibilities from mixed states by a longer pulse scheme. The coherence decay during longer sequences arises from the saturation of the state’s complexity, while the deviation from the theory occurs from general decoherence (e.g., from motional heating and magnetic field fluctuations) and the accumulation of small pulse-to-pulse control errors.

This experiment demonstrates *phase-insensitive robustness* to stable-but-unknown phases that enables hardware-efficient qubit-parity quantum processing. Rather than relying on active correction, it can be exported to other platforms and more complex experiment which may inspire new approaches to building robust quantum components. Our work thus opens several immediate avenues for future research. It joins a broad effort into generating macroscopic quantum states, analogous to Schrödinger’s cat, pioneered in cavity QED with microwave photons [36] and extended to numerous platforms, including propagating optical fields [37–39], integrated photonic architectures [40], or mechanics of trapped ions [21, 41]. A direct extension of our experiment would be to create “multimode” states by entangling the qubit with several distinct motional modes of the same ion, a key step towards engineering complex oscillator states [17, 42]. While recent work has demonstrated resilience to initial state imperfections (thermal noise) [32], our approach addresses a complementary challenge: resilience to uncontrolled interaction dynamics. Together, these methods provide a pathway for robust quantum control in non-ideal environments. Building on these foundations, the principle of phase-insensitive entanglement could then be applied to a collective motional mode of a multi-ion crystal. This would provide a powerful tool for the robust generation of multi-qubit entangled states, such as GHZ states [43, 44], whose creation is typically highly sensitive to the precise control of laser phases. Furthermore, this technique provides a powerful tool for creating and manipulating unexplored Schrödinger’s cat states, for example by using higher order sideband interactions. This would broaden the accessibility of complex quantum phenomena for both fundamental exploration and, potentially, technological application.

## ACKNOWLEDGMENT

K.S., K.P., L.S. and R.F. have been supported by the project GA22-27431S of the Czech Science Foundation. K.S., K.P., V.S., A.K., L.S. and R.F. also acknowledge project CZ.02.01.01/00/22\_008/0004649 (QUEENTEC) of EU and MEYS Czech Republic. R.F. also used support from the project No. LUC25006 of MEYS Czech Republic.

## AUTHOR CONTRIBUTIONS

R.F. developed the theory idea and conceived the project. K.P., R.F., and L.S. developed the idea about the measurement and verification, and K.P. performed analytical and numerical calculations with inputs about evaluation and interpretation from R.F.. K.P. wrote the manuscript with inputs from R.F. and contributions of all authors. K.S. and V.S. performed the experiment and analyzed the experimental data under the supervision of L.S..

### Appendix A: Data Reconstruction with a decoherence Model

While these panels show the coherence projected onto specific measurement axes, the state's total coherence is manifested by the maximum interference amplitude (the global maximum of  $P_g$  minus the global minimum) over the full two-dimensional phase space of  $(\phi_1, \phi_2)$ , as in Appendix E. As quantitatively validated in Appendix E for general parity-entangled states, a Fourier decomposition of this signal  $P_g(\phi_1, \phi_2)$  allows us to isolate and measure specific, multi-order coherence terms ( $|n\rangle\langle m|$ ), and the contrast over verification pulse phases measures the total coherence, up to certain order  $|m - n| \leq 3$ .

We verify our success by reconstructing the experimental data using a theoretical model that incorporates a single decoherence parameter,  $w$  (see Eq. (D4) and Appendix C). As shown in Figures A.1 and 4, this model faithfully reproduces the experimental data. Figure A.2 presents the measured phonon number distributions  $P(n)$  and the corresponding visibility of the interference fringes for states prepared with  $N = 2, 3$ , and 4 pulses. The visibility is plotted as a function of the first verification pulse phase,  $\phi_1$ , after averaging over the second phase,  $\phi_2$ . The solid lines represent the predictions from our theoretical model using a single fitted decoherence parameter,  $w$ , for each case. The excellent agreement between the experimental data (points) and the model (lines) across different state complexities validates our core claim: the experiment reliably generates the target qubit-parity entangled state, and its partial coherence can be accurately characterized.

### Appendix B: Minimal example of preparation and verification

Our minimal experiment outlines expandable steps demonstrating basic principles, ensuring even basic experimental setups can clearly show coherence and increased macroscopicity. These principles extend to the longer sequences used in the experiment. Below, B (R) represents a blue (red) sideband pulse; “|” separates preparation and verification.

$B/R, B/B$  ( $N = 1$ ): The minimal modulation demonstration in verification scans occurs even at  $N = 1$ . Single blue pulses are used in both preparation and verification, with the phase of the verification pulse being scanned. The input state  $|g, 0\rangle$  evolves after a preparation blue pulse (and

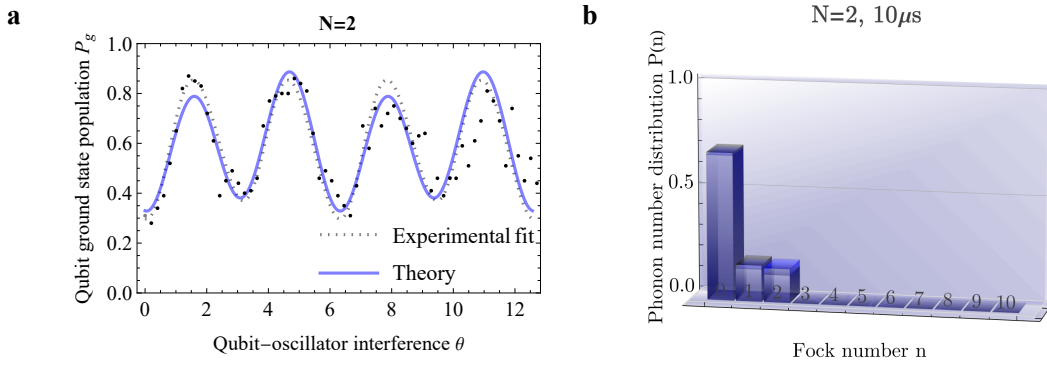


Figure A.1. **Reconstruction of experimental data for an  $N = 2$  state.** The experimental data (points) are successfully reproduced by a theoretical model (solid lines and surface) incorporating a single fitted decoherence parameter ( $w \approx 0.95$ ). **a** Ramsey-like fringe decay, showing coherence. **b** Reconstructed phonon number distribution  $P(n)$  from Rabi flop measurements, with a mean phonon number  $\langle \hat{n} \rangle = 0.475$ .

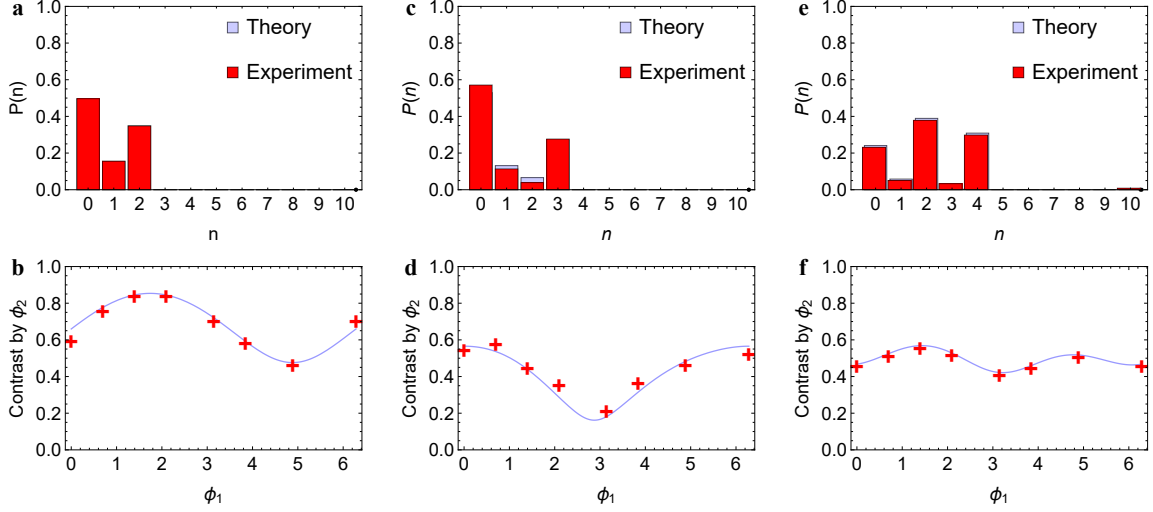


Figure A.2. **a,c,e**  $P(n)$  data from experiments and from theoretical description (using fitted parameters), and **b,d,f** corresponding  $P_g$  modulation contrast vs  $\phi_1$  (averaged over  $\phi_2$ ) for various  $N$  for various verification pulse phases. (**a,b**  $N = 2$ , **c,d**  $N = 3$ , **e,f**  $N = 4$ ).

global phase) to:

$$|\Psi\rangle_B = \cos\left[\frac{t_1}{2}\right] |g, 0\rangle + e^{i(\theta+\varphi_1)} \sin\left[\frac{t_1}{2}\right] |e, 1\rangle. \quad (\text{B1})$$

$t_1$  is the preparation pulse length (area). The coherence phase  $\theta$  is associated with the laser phase  $\phi_1$ .

Scanning the phase of a red verification pulse does not create detection modulation, as it transfers population from  $|e, 1\rangle$  to  $|g, 2\rangle$ . A red verification pulse (phase  $\phi_1$ , length  $t_R$ ) acting on  $|\Psi\rangle_B$  yields:

$$|\Psi\rangle_{B|R} = \cos\left[\frac{t_1}{2}\right] |g, 0\rangle + e^{i(\theta+\phi_1)} \sin\left[\frac{t_1}{2}\right] \cos\left[\frac{t_R}{\sqrt{2}}\right] |e, 1\rangle + \sin\left[\frac{t_1}{2}\right] e^{i(\theta+\varphi_1-\phi_1)} \sin\left[\frac{t_R}{\sqrt{2}}\right] |g, 2\rangle. \quad (\text{B2})$$

Due to the orthogonality of the oscillator states, qubit ground state weight  $P_g$  is not modulated by  $\phi_1$ . In contrast, a blue verification pulse (phase  $\phi_1$  and pulse length  $t_B$ ) yields:

$$\begin{aligned} |\Psi\rangle_{B|B} = & \left( e^{i(\theta+\phi_1)} \sin\left[\frac{t_1}{2}\right] \cos\left[\frac{t_B}{2}\right] - \cos\left[\frac{t_1}{2}\right] e^{i\phi_1} \sin\left[\frac{t_B}{2}\right] \right) |e, 1\rangle \\ & + \left( \cos\left[\frac{t_1}{2}\right] \cos\left[\frac{t_B}{2}\right] + \sin\left[\frac{t_1}{2}\right] e^{i(\theta+\varphi_1-\phi_1)} \sin\left[\frac{t_B}{2}\right] \right) |g, 0\rangle. \end{aligned} \quad (\text{B3})$$

Due to the relative phase  $\varphi_1 - \phi_1$ , ground state probability  $P_g$  modulates due to interference between  $|g, 0\rangle$  and  $|e, 1\rangle$ . Maximum interference amplitude is 1 at  $t_1 = t_{R,B} = \frac{\pi}{2}$ , where the prepared state (B1) has an oscillator energy of  $1/2$ . If an incoherent state  $\rho = \cos^2[\frac{t_1}{2}] |g, 0\rangle \langle g, 0| + \sin^2[\frac{t_1}{2}] |e, 1\rangle \langle e, 1|$  was prepared (instead of  $|\Psi\rangle_B$ ), no modulation occurs.

The final ground state probability  $P_g$  is given by:

$$P_g = \frac{1}{2} \left( 1 + \cos(t_1) \cos(t_B) - w \sin(t_1) \sin(t_B) \cos(\varphi_1 - \phi_1) \right). \quad (\text{B4})$$

Here, the modulation amplitude is directly proportional to the coherence factor  $w$ . An ideal, perfectly coherent state ( $w = 1$ ) would yield the maximum possible visibility. The experimentally observed visibility of 0.4 therefore allows for a direct estimation of the state's coherence, indicating that  $w \approx 0.9$ . By independently measuring the state's populations, we can disentangle the loss of coherence (captured by  $w$ ) from imperfections in the verification pulse itself. Conversely, the modulation amplitude depends linearly on the coherence factor  $w$ . This provides a general method for its determination: first, the Fock state populations  $|c_n|^2 = P(n)$  are measured independently. From these populations and a

given verification pulse length  $t'$ , the expected modulation amplitude for a perfectly coherent state ( $w = 1$ ) can be calculated, using Fourier series expansion. By comparing this ideal amplitude to the experimentally measured amplitude, we can directly estimate the true coherence factor  $w$ .

$BR/R$ ,  $BR/B$  ( $N = 2$ ) : After preparation pulses with a second red pulse (phase  $\phi_2$ ), the prepared state with the mutual phase encoding is:

$$|\Psi\rangle_{BR} = \cos\left[\frac{t_1}{2}\right] |g, 0\rangle - ie^{i(\varphi_1 + \theta + \frac{\pi}{2})} \sin\left[\frac{t_1}{2}\right] \cos\left[\frac{t_2}{\sqrt{2}}\right] |e, 1\rangle - e^{i(\varphi_1 - \varphi_2)} \sin\left[\frac{t_1}{2}\right] \sin\left[\frac{t_2}{\sqrt{2}}\right] |g, 2\rangle. \quad (\text{B5})$$

After red verification pulse, the state evolves to

$$|\Psi\rangle_{BR|R} = \cos\left[\frac{t_1}{2}\right] |g, 0\rangle + e^{i(\varphi_1 - \varphi_2)} \sin\left(\frac{t_1}{2}\right) \left( e^{i(\theta + \varphi_2)} \cos\left(\frac{t_2}{\sqrt{2}}\right) \cos\left(\frac{t_R}{\sqrt{2}}\right) + \sin\left(\frac{t_2}{\sqrt{2}}\right) e^{i\phi_1} \sin\left(\frac{t_R}{\sqrt{2}}\right) \right) |e, 1\rangle \\ + e^{i\varphi_1} \sin\left(\frac{t_1}{2}\right) \left( \cos\left(\frac{t_2}{\sqrt{2}}\right) e^{i(\theta - \varphi_1)} \sin\left(\frac{t_R}{\sqrt{2}}\right) - e^{-i\varphi_2} \sin\left(\frac{t_2}{\sqrt{2}}\right) \cos\left(\frac{t_R}{\sqrt{2}}\right) \right) |g, 2\rangle. \quad (\text{B6})$$

Maximum interference for this state occurs when the verification pulse couples the dominant motional components, in this case  $|g, 2\rangle$  and  $|e, 1\rangle$ . The magnitude of this interference is reduced if the initial state preparation is imperfect (e.g., if population remains in the vacuum state).

With decoherence factor  $w$ ,  $P_g$  modulation by  $\phi_1$ :

$$P_g = \frac{1}{4} \left( 2 \sin^2\left(\frac{t_1}{2}\right) \left( -(w-1) \sin(\sqrt{2}t_2) \sin(\sqrt{2}t_R) \cos(\varphi_2 - \phi_1) - \cos(\sqrt{2}t_2) \cos(\sqrt{2}t_R) \right) + \cos(t_1) + 3 \right). \quad (\text{B7})$$

Again, only modulation amplitude depends linearly on  $w$ . From known  $P(n)$ ,  $t'_1$  can be precisely specified from the non-modulating value, and thus  $w$  precisely determined.

After blue verification pulse (instead of red), the state evolves to

$$|\Psi\rangle_{BR|B} = \left( \cos\left(\frac{t_1}{2}\right) \cos\left(\frac{t_B}{2}\right) + \sin\left(\frac{t_1}{2}\right) \cos\left(\frac{t_2}{\sqrt{2}}\right) e^{i(\varphi_1 + \theta - \phi_1)} \sin\left(\frac{t_B}{2}\right) \right) |g, 0\rangle \\ - e^{i(\varphi_1 - \varphi_2)} \sin\left(\frac{t_1}{2}\right) \sin\left(\frac{t_2}{\sqrt{2}}\right) \cos\left(\frac{1}{2}\sqrt{3}t_B\right) |g, 2\rangle \\ + \left( e^{i(\varphi_1 + \theta)} \sin\left(\frac{t_1}{2}\right) \cos\left(\frac{t_2}{\sqrt{2}}\right) \cos\left(\frac{t_B}{2}\right) - \cos\left(\frac{t_1}{2}\right) e^{i\phi_1} \sin\left(\frac{t_B}{2}\right) \right) |e, 1\rangle \\ + \sin\left(\frac{t_1}{2}\right) \sin\left(\frac{t_2}{\sqrt{2}}\right) e^{i(\phi_1 + \varphi_1 - \varphi_2)} \sin\left(\frac{1}{2}\sqrt{3}t_B\right) |e, 3\rangle. \quad (\text{B8})$$

Here, the last pulse exhibits the interference of  $|g, 0\rangle \leftrightarrow |e, 1\rangle$ . In both cases, we again see the equivalence of varying  $\phi_1$  and  $\theta$ .

### Appendix C: Effect of sideband pulses

The effect of the  $j$ -th red pulse ( $l = -1$ ) or blue pulse ( $l = 1$ ) is described by a unitary transformation  $U_l^{(j)}$ , as detailed in [28]:

$$U_l^{(j)} |\Psi\rangle^{(j-1)} = \sum_{n=\text{even}} \left( c_{l+n}^{(j-1)} \cos\left(\frac{t\Omega_{n,n+l}}{2}\right) - ie^{i(\phi + \frac{\pi}{2})} c_n^{(j-1)} \sin\left(\frac{t\Omega_{n,n+l}}{2}\right) \right) |e, n+l\rangle \\ + \left( c_n^{(j-1)} \cos\left(\frac{t\Omega_{n,n+l}}{2}\right) - ie^{i(\phi + \frac{\pi}{2})} c_{l+n}^{(j-1)} \sin\left(\frac{t\Omega_{n,n+l}}{2}\right) \right) |g, n\rangle, \quad (\text{C1})$$

where  $\eta$  is the Lamb-Dicke parameter, and  $\Omega_{n,n+l} = \eta\Omega_0\sqrt{n + \frac{l+1}{2}}$  is the Rabi frequency, with  $\Omega_0$  being the fundamental Rabi frequency. The coefficients  $c_n^{(j-1)}$  are determined by the preceding  $j-1$  pulses. This transformation applies to all pulses, including those used for verification. The pulse area, the integrated area under the applied pulse envelope, is a function of both the pulse strength (amplitude) and the pulse duration (length). We assume the Rabi frequency to be time-independent.

### Appendix D: Effect of decoherence and determination of the coherence parameter $w$

A physically motivated model for decoherence assumes that off-diagonal terms in the density matrix,  $|n\rangle\langle m|$ , decay at a rate dependent on their separation  $k = |n - m|$ . This captures that long-range coherences are more fragile. Under a model of independent, local dephasing events, the coherence of each term in the density matrix of the ideal prepared state,  $\rho^{(\text{ideal})}$ , would be suppressed exponentially:

$$\rho_{nm} = \rho_{nm}^{(\text{ideal})} w^{|n-m|}, \quad (\text{D1})$$

where the parameter  $w \leq 1$  represents the fundamental coherence factor between adjacent Fock states.

However, as detailed in Appendix G, our two-pulse verification sequence is primarily sensitive only to short-range coherences where  $|n - m| \leq 3$ . For a state with a high degree of overall coherence ( $w \approx 1$ ), the suppression factors for these relevant terms ( $w$ ,  $w^2$ , and  $w^3$ ) are all numerically close. Therefore, for the practical analysis in this work, we can simplify this picture by adopting a single *effective* coherence parameter, which we also denote as  $w$ . This single parameter effectively captures the average suppression of the specific off-diagonal terms that our measurement probes.

This simplification allows us to model the state with a single parameter that directly relates to the observed interference contrast. The partially coherent state is written as an incoherent mixture of the ideal pure state  $|\Psi\rangle$  and its fully dephased version:

$$\rho[w] = w|\Psi\rangle\langle\Psi| + (1-w)\text{diag}[|\Psi\rangle\langle\Psi|], \quad (\text{D2})$$

where  $\text{diag}[\rho]$  is the matrix containing only the diagonal elements of  $\rho$ . The modulation amplitude in our interference measurements is then suppressed by this effective factor  $w$  relative to the ideal coherent case ( $w = 1$ ). This type of state can result from the combined effect of qubit dephasing and oscillator dephasing, modeled here phenomenologically. The other type of state model with diminished mutual information is

$$\rho[w] = w|\Psi\rangle\langle\Psi| + (1-w)\left(\frac{1}{2}|e\rangle\langle e| \otimes |\psi_-\rangle\langle\psi_-| + \frac{1}{2}|g\rangle\langle g| \otimes |\psi_+\rangle\langle\psi_+|\right), \quad (\text{D3})$$

where  $|\psi_{\pm}\rangle$  are even/odd states associated to each qubit basis. Dominant physical mechanisms contributing to the reduction of  $w$  (i.e., an increase in the incoherent fraction  $1 - w$ ) in our trapped ion system include motional heating from noisy trap potentials or patch potentials [45], uncompensated slow laser phase/frequency noise, and magnetic field fluctuations that cause shot-to-shot variations in the prepared state's relative phase  $\theta$ . For the macroscopic motional states explored, motional heating and such environmental phase drifts are expected to be primary contributors. For the full decoherence models, we should use the descriptions as in [35].

Similar suppression of the verification pulse phase modulation contrast can also occur if the Ramsey pulse length  $t_{R,B}$  is small. To exclude these effects, we employ a multi-step analysis. First, the Fock distribution  $P(n)$  measured via Rabi flopping (Sec II.c) constrains the prepared state amplitudes  $|c_n|$ . Second, the average value of  $P_g$  over the verification phase scans depends on  $|c_n|^2$  and the verification pulse lengths  $t_{R,B}$  (via terms like Eq. D5 and its two-pulse extension), allowing  $t_{R,B}$  to be estimated. Finally, the amplitude of the observed  $P_g$  modulation (dependent on terms like Eq. D6) is compared to the amplitude expected for the estimated  $c_n$  and  $t_{R,B}$  in the ideal coherent case ( $w = 1$ ), allowing the coherence factor  $w$  to be determined. This disentanglement of  $w$  from errors in  $t_{R,B}$  relies on  $t_{R,B}$  primarily affecting the average population transfer (DC offset of  $P_g$ ) and overall scaling of modulation, while  $w$  specifically scales the relative amplitude of the coherent interference terms. The robustness of this separation can be challenged if decoherence during preparation significantly alters  $P(n)$  itself, as this affects the  $|c_n|$  used to estimate  $t_{R,B}$ , potentially leading to propagated errors. However, the distinct mathematical dependencies generally allow for their separate estimation, assuming errors in  $t_{R,B}$  do not systematically mimic the phase-dependent signatures of coherence loss captured by  $w$ . A brief sensitivity analysis indicates that a typical 1% mismatch in the driving field strength (affecting the Rabi frequency  $\Omega$ ) and thus the verification pulse area  $t_{R,B}$ , cause the subsequent impact on the estimated coherent fraction  $w$  is correspondingly small by approximately 1-2%, supporting the robustness of this disentanglement under typical experimental imperfections.

Consider a prepared state in a partially coherent mixture:

$$\rho_{\Psi}[w] \equiv w|\Psi\rangle\langle\Psi| + (1-w)\text{diag}[|\Psi\rangle\langle\Psi|], \quad (\text{D4})$$

where  $|\Psi\rangle = \sum_n c_n |f_n, n\rangle$  (real coefficients  $c_n = |c_n|e^{i\phi_n}$ , and  $|f_n\rangle$  can be either  $|e\rangle$  or  $|g\rangle$  depending on the number parity of  $n$ ). The modulation amplitude is suppressed by  $w$ , and so are the contrast

and the visibility, for a general state  $\rho_\Psi[w]$ . For a red sideband verification pulse, the non-modulating term of  $P_g$  (w.r.t. pulse phase) is:

$$\sum_{n=\text{even}} |c_n|^2 \cos^2 \left( \frac{\sqrt{n/2}}{\sqrt{2}} t_R \right) + \sum_{n=\text{odd}} |c_n|^2 \sin^2 \left( \frac{\sqrt{(n+1)/2}}{\sqrt{2}} t_R \right). \quad (\text{D5})$$

The non-modulating term Eq. (D5) can be predicted solely from the measured populations  $P(n) \approx |c_n|^2$ . Modulation amplitude is:

$$w \left| \sum_{n=1} c_{2n-1} c_{2n} e^{i(\varphi_{2n} - \varphi_{2n-1})} \sin \left( \sqrt{2n} t_R \right) \right|. \quad (\text{D6})$$

The modulation amplitude Eq. (D6) is then measured, and by comparing it to the ideal case ( $w = 1$ ), we can extract the coherence factor  $w$  for the prepared state. The above derivation shows that the amplitude of the measured interference fringes is directly proportional to  $w$ , making it a direct experimental signature of the state's quantum coherence.

The values of the coherent fraction  $w$  that explain the experimental data best using this procedure are given as: For a setup of  $N = 1, 2, 3, 4, 6$ ,  $1 - w \approx 0.05, 0.04 - 0.12, 0.083, 0.137 - 0.143$  and  $0.08 - 0.13$ . For longer preparation pulse sequences, determination of  $w$  has more uncertainty due to the existence of many parameters and potential propagation of errors in the estimation. For  $N = 8, 10, 12$ , the incoherence fraction is about  $1 - w \approx 0.08 - 0.13, 0.09 - 0.2, 0.08 - 0.13$ . These values indicate a generally high degree of coherence. The observed complex scaling of  $1 - w$  with the number of pulses  $N$  suggests an interplay of multiple physical mechanisms. Plausible contributions include time-dependent effects such as motional heating and qubit dephasing, which accumulate over the sequence duration, and pulse-dependent errors from laser imperfections that accumulate with each operation. The non-trivial scaling likely arises because the growing macroscopic state becomes differentially sensitive to these error channels. A detailed analysis to disentangle these contributions would be a valuable next step but is beyond the scope of this work. This complexity influences the ultimate scalability of preparing highly coherent macroscopic states.

**Verification of off-diagonal elements** Alternatively, we can analyze the coherence structure in the frequency domain. Each off-diagonal element of the prepared state's density matrix, such as  $|n\rangle\langle m|$ , contributes to the modulation of  $P_g$  at a unique frequency with respect to the verification phases  $\phi_1$  and  $\phi_2$ . This allows us to use Fourier analysis of the measured  $P_g(\phi_1, \phi_2)$  signal to identify the presence and magnitude of specific coherence terms. In order for them to have measurable effects, the verification pulses must coherently couple the relevant states before measurement.

Experimentally, we can observe such effects by analyzing the frequency components of the  $P_g$  modulation as a function of  $\phi_1$  and  $\phi_2$ . For example, as detailed in Appendix F, a coherence term like  $|g, 0\rangle\langle e, 3|$  (representing coherence between states differing by 3 phonons) will uniquely generate a modulation signal at a frequency proportional to  $2\phi_1 + \phi_2$  under an RSB-BSB verification sequence. Observing a signal at this specific frequency is therefore direct evidence of this "deep" coherence element. While potentially challenging to measure due to small coefficients, observing modulation at the corresponding frequency provides a signature consistent with such deep coherence. Therefore, using the characteristic modulation frequencies, we can distinguish the effects and signatures of the prepared off-diagonal elements.

By performing a Fourier analysis of the measured  $P_g(\phi_1, \phi_2)$  data, we can identify signatures of specific off-diagonal coherence terms. For the  $N = 3$  state, we detect a non-zero modulation amplitude at the frequency corresponding to the  $|g, 0\rangle\langle e, 3|$  coherence. The fitted amplitude of this signal is 0.105, in close agreement with the ideal theoretical prediction of 0.095, confirming the presence of this long-range coherence. Similarly, for  $N = 4$ , we detect a small but non-zero signature for the  $|e, 1\rangle\langle g, 4|$  coherence. The existence of these specific, higher-order coherence terms provides definitive, quantitative evidence of the complex entangled structure created by our method. The detection of these non-zero Fourier coefficients is a direct measurement of higher-order coherence within the prepared state.

## Appendix E: Derivation of the orthogonal mapping between coherence and probe phases

This section provides the mathematical derivation for the measurement method used in the main text. We demonstrate how the coherence of the prepared state  $|\Psi\rangle$ , parameterized by the qubit-

oscillator phase  $\theta$  and the internal oscillator phase  $\Theta$ , can be independently measured by controlling the external phases  $\phi_1$  and  $\phi_2$  of the verification pulses. We show that the commutation relations of the phase rotation and sideband interaction operators create an orthogonal mapping, where the sum of the probe phases  $\frac{\phi_1 + \phi_2}{2}$  addresses  $\theta$ , and the difference  $\frac{\phi_1 - \phi_2}{2}$  addresses  $\Theta$ .

The commutation relations between phase rotation operators and the evolution operator induced by sideband pulses illustrate the mapping between internal coherence and the phase of verification pulses. Specifically, the transformation under the qubit rotation operator for the red sideband interaction is given by:

$$\exp [i\kappa(\sigma_+ \hat{a} e^{-i\phi} + \sigma_- \hat{a}^\dagger e^{i\phi})] \exp \left[ i\frac{\theta}{2} \sigma_z \right] = \exp \left[ i\frac{\theta}{2} \sigma_z \right] \exp \left[ i\kappa(\sigma_+ \hat{a} e^{-i(\theta + \phi)} + \sigma_- \hat{a}^\dagger e^{i(\theta + \phi)}) \right]. \quad (\text{E1})$$

This shows the effect of a qubit phase rotation on the red sideband (RSB) interaction. Physically, this demonstrates that applying a qubit rotation corresponding to phase  $\theta$  *before* the interaction is mathematically identical to shifting the external laser phase  $\phi$  by  $+\theta$  *during* the interaction.

Similarly, the adjoint relation for oscillator coherence by oscillator phase rotation operation:

$$\exp [i\kappa(\sigma_+ \hat{a} e^{-i\phi} + \sigma_- \hat{a}^\dagger e^{i\phi})] \exp [i\Theta \hat{n}] = \exp [i\Theta \hat{n}] \exp \left[ i\kappa(\sigma_+ \hat{a} e^{-i(-\Theta + \phi)} + \sigma_- \hat{a}^\dagger e^{i(-\Theta + \phi)}) \right]. \quad (\text{E2})$$

Conversely, this equation shows the effect of a motional phase rotation. This transformation is equivalent to shifting the external laser phase  $\phi$  by  $-\Theta$ . The opposite sign of this phase shift compared to the qubit rotation is the fundamental reason our method can distinguish the two types of coherence.

Analogous transformations apply to blue sideband pulses. Explicitly,

$$\exp [i\kappa(\sigma_+ \hat{a}^\dagger e^{-i\phi'} + \sigma_- \hat{a} e^{i\phi'})] \exp \left[ i\frac{\theta}{2} \sigma_z \right] = \exp \left[ i\frac{\theta}{2} \sigma_z \right] \exp \left[ i\kappa(\sigma_+ \hat{a}^\dagger e^{-i(\theta + \phi')} + \sigma_- \hat{a} e^{i(\theta + \phi')}) \right]. \quad (\text{E3})$$

Similarly, the adjoint relation for oscillator coherence by oscillator phase rotation operation:

$$\exp [i\kappa(\sigma_+ \hat{a}^\dagger e^{-i\phi'} + \sigma_- \hat{a} e^{i\phi'})] \exp [i\Theta \hat{n}] = \exp [i\Theta \hat{n}] \exp \left[ i\kappa(\sigma_+ \hat{a}^\dagger e^{-i(\Theta + \phi')} + \sigma_- \hat{a} e^{i(\Theta + \phi')}) \right]. \quad (\text{E4})$$

These equations show the analogous transformations for a blue sideband (BSB) pulse. Crucially, for a BSB interaction, both the qubit rotation ( $\theta$ ) and the motional rotation ( $\Theta$ ) result in a shift of the *same sign* ( $+\theta$  and  $+\Theta$ ) in the external phase  $\phi'$ . The difference in how the motional phase  $\Theta$  affects RSB versus BSB pulses is what allows for the orthogonal mapping. These operator identities demonstrate that the internal coherence phases of the state ( $\theta$ ,  $\Theta$ ) and the external control phases of the verification pulses ( $\phi_1$ ,  $\phi_2$ ) are interchangeable. When we apply a two-pulse verification sequence (e.g., RSB with phase  $\phi_1$  followed by BSB with phase  $\phi_2$ ), the total phase dependence of the final state arises from combinations of these shifts. The qubit-oscillator coherence  $\theta$  will manifest in terms dependent on  $(\phi_1 + \phi_2)/2$  because its effect has the same sign for both pulses. In contrast, the internal oscillator coherence  $\Theta$  will manifest in terms dependent on  $(\phi_1 - \phi_2)/2$  because its effect has the opposite sign for RSB versus BSB pulses.

Consequently, the probability of qubit ground state  $P_g$  from the prepared state  $\sum_{j=0}^N c_j |f(j), j\rangle$  where  $f(j) = e, g$  depending on the parity of Fock number  $j$  after the verification pulses (e.g., RSB( $\phi_1$ ) then BSB( $\phi_2$ )) acting on the prepared state  $|\Psi\rangle$  can be written schematically as

$$P_g = \text{const} + \sum_{k,l} A_{kl} \cos(k\phi_1 + l\phi_2) + B_{kl} \sin(k\phi_1 + l\phi_2) \quad (\text{E5})$$

The amplitudes of the oscillating terms,  $A_{kl}$  and  $B_{kl}$ , are directly proportional to the magnitude of the coherence in the prepared state, while the phase offsets of the fringes reveal the internal phases  $\theta$

and  $\Theta$ . Under the partial coherence model (Eq. D4), this functional form is still maintained, while the amplitudes of the oscillating terms ( $A_{kl}, B_{kl}$ ) are linearly diminishing by  $w$ .

Applying a second verification pulse allows for a more detailed analysis. To be more concrete, we can explicitly write down the Positive Operator-Valued Measure (POVM) element  $\Pi$  corresponding to a final measurement of the qubit in the ground state  $|g\rangle$ . For an RSB( $\phi_1$ )-BSB( $\phi_2$ ) verification sequence, this operator can be decomposed into three terms,  $\Pi = \Pi_1 + \Pi_2 + \Pi_3$ , which describe the different physical processes contributing to the final  $P_g$ .

$$\hat{\Pi}_3 = \sum_{k=1} -\frac{1}{2} |e\rangle \langle g| \otimes |2k-1\rangle \langle 2(k+1)| \exp[i(2\phi_1 - \phi_2)] \sin(\sqrt{2k+1}t'_2) \sin\left(\sqrt{\frac{k}{2}}t'_1\right) \sin\left(\sqrt{\frac{k+1}{2}}t'_1\right), \quad (\text{E6})$$

This term contains the operator  $|e\rangle \langle g|$  and describes transitions between the two qubit states. It is responsible for probing the *qubit-oscillator coherence of the third order Fock coherence*. For  $t'_2 = 0$ , this term reduces to 0.

$$\begin{aligned} \hat{\Pi}_2 = & |g\rangle \langle g| \otimes \sum_{k=1} -\frac{1}{2} |2(k-1)\rangle \langle 2(k+1)| \exp[i(\phi_1 - \phi_2)] \sin(\sqrt{2k-1}t'_2) \cos\left(\sqrt{\frac{k-1}{2}}t'_1\right) \sin\left(\sqrt{\frac{k}{2}}t'_1\right) \\ & + |e\rangle \langle e| \otimes \sum_{k=1} \frac{1}{2} |2k-1\rangle \langle 2k+1| \exp[i(\phi_1 - \phi_2)] \sin(\sqrt{2k+1}t'_2) \cos\left(\sqrt{\frac{k+1}{2}}t'_1\right) \sin\left(\sqrt{\frac{k}{2}}t'_1\right). \end{aligned} \quad (\text{E7})$$

This term contains operators like  $|g\rangle \langle g|$  and  $|e\rangle \langle e|$ , describing transitions within the same qubit subspace. It therefore probes the *internal oscillator coherence* within each parity subspace. For  $t'_2 = 0$ , this term is reduced to 0 as well. This term remains constant for  $\phi_1 - \phi_2 = \text{const}$ .

$$\begin{aligned} \hat{\Pi}_1 = & |g\rangle \langle e| \otimes \sum_{k=1} \frac{1}{2} |2k-2\rangle \langle 2k-1| \exp[-i\phi_2] \sin(\sqrt{2k-1}t'_2) \cos\left(\sqrt{\frac{k-1}{2}}t'_1\right) \cos\left(\sqrt{\frac{k}{2}}t'_1\right) \\ & - |e\rangle \langle g| \otimes \sum_{k=1} \frac{1}{2} |2k-1\rangle \langle 2k| \exp[i\phi_1] \sin(\sqrt{2k}t'_1) \times \left[ \sin^2\left(\frac{\sqrt{2k-1}}{2}t'_2\right) - \cos^2\left(\frac{\sqrt{2k+1}}{2}t'_2\right) \right]. \end{aligned} \quad (\text{E8})$$

This term also contributes to the interference signal, representing cross-terms in the measurement. This term can be detected by the single-pulse measurement, i.e. when  $t'_2 = 0$ . It then reduces to

$$\hat{\Pi}_1 = -|e\rangle \langle g| \otimes \sum_{k=1} \frac{1}{2} |2k-1\rangle \langle 2k| \exp[i\phi'_1] \sin(\sqrt{2k}t'_1). \quad (\text{E9})$$

These are substituted directly into the following probabilities. The expression for the term containing  $\exp[3i\Theta]$  is given by:

$$P_g^{(3)} = \sum_{k=1} -\frac{1}{2} c_{2(k+1)} c_{2k-1}^* \exp[i(2\phi'_1 - \phi'_2)] \sin(\sqrt{2k+1}t'_2) \sin\left(\sqrt{\frac{k}{2}}t'_1\right) \sin\left(\sqrt{\frac{k+1}{2}}t'_1\right). \quad (\text{E10})$$

The expression for the term containing  $\exp[2i\Theta]$  is given by:

$$\begin{aligned} P_g^{(2)} = & \sum_{k=1} -\frac{1}{2} c_{2(k+1)} c_{2(k-1)}^* \exp[i(\phi'_1 - \phi'_2)] \sin(\sqrt{2k-1}t'_2) \cos\left(\sqrt{\frac{k-1}{2}}t'_1\right) \sin\left(\sqrt{\frac{k}{2}}t'_1\right) \\ & + \frac{1}{2} c_{2k+1} c_{2k-1}^* \exp[i(\phi'_1 - \phi'_2)] \sin(\sqrt{2k+1}t'_2) \cos\left(\sqrt{\frac{k+1}{2}}t'_1\right) \sin\left(\sqrt{\frac{k}{2}}t'_1\right). \end{aligned} \quad (\text{E11})$$

The expression for the term containing  $\exp[i\Theta]$  is given by:

$$P_g^{(1)} = \sum_{k=1} \frac{1}{2} c_{2k-1} c_{2k-2}^* \exp[-i\phi_2'] \sin(\sqrt{2k-1}t_2') \cos\left(\sqrt{\frac{k-1}{2}}t_1'\right) \cos\left(\sqrt{\frac{k}{2}}t_1'\right) - \frac{1}{2} c_{2k} c_{2k-1}^* \exp[i\phi_1'] \sin(\sqrt{2k}t_1') \times \left[ \sin^2\left(\frac{\sqrt{2k-1}}{2}t_2'\right) - \cos^2\left(\frac{\sqrt{2k+1}}{2}t_2'\right) \right]. \quad (\text{E12})$$

The terms depending on  $\exp[-ik\Theta]$  for  $k = 1, 2, 3$  is given simply by their complex conjugates. The non-modulating (DC) component of  $P_g$  for a two-pulse sequence is given by:

$$\sum_{n=\text{even}} |c_n|^2 \left( \cos\left[\frac{\sqrt{n+1}}{2}t_2'\right] \cos\left[\frac{\sqrt{n}}{2}t_1'\right]^2 + \sin\left[\frac{\sqrt{n-1}}{2}t_2'\right]^2 \sin\left[\frac{\sqrt{n}}{2}t_1'\right]^2 \right) + \sum_{n=\text{odd}} |c_n|^2 \left( \cos\left[\frac{\sqrt{n+2}}{2}t_2'\right] \sin\left[\frac{\sqrt{n+1}}{2}t_1'\right]^2 + \sin\left[\frac{\sqrt{n}}{2}t_2'\right]^2 \cos\left[\frac{\sqrt{n+1}}{2}t_1'\right]^2 \right). \quad (\text{E13})$$

As before, this DC term depends on the measured populations and the known verification pulse area  $(t_1', t_2')$ , while the modulation amplitude depends linearly on the coherence factor  $w$ , allowing for its robust estimation. Non-zero co-existence of  $P_g^{(1)}$ ,  $P_g^{(2)}$  and  $P_g^{(3)}$  signifies the complex structure in Fock basis, minimally containing terms of  $\{|0\rangle, |1\rangle, |3\rangle\}$ , which can be directly measured by the Fourier series expansion of the total probability  $P_g$ . By varying verification pulse area  $(t_1', t_2')$ , it is also possible to explore individual coherence of  $|n\rangle\langle m|$  for different  $n, m$ .

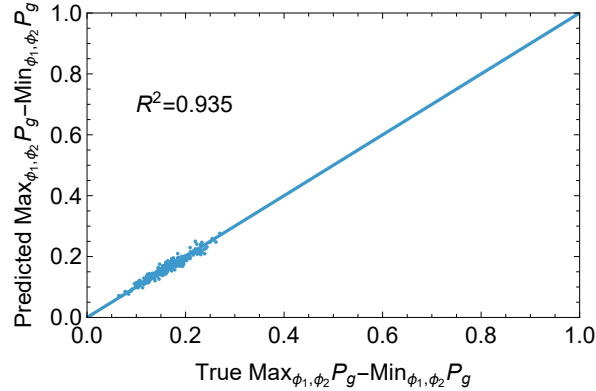


Figure E.1. **Quantitative validation of the coherence model.** Scatter plot of the predicted maximum interference amplitude versus the true measured amplitude for a wide range of prepared states. The “True Max” (horizontal axis) is the total contrast ( $P_{\max} - P_{\min}$ ) extracted directly from numerical simulation by scanning the verification phases  $\phi_1$  and  $\phi_2$ . The “Predicted Max” (vertical axis) is using the magnitudes of the dominant Fourier components of the interference signal,  $P_g^{(1)}$ ,  $P_g^{(2)}$ ,  $P_g^{(3)}$ , as defined in Eqs. (D6-D8). The strong linear correlation, with a coefficient of determination  $R^2 \approx 0.94$ , provides direct quantitative proof that the contrast is largely determined by the underlying multi-pathway quantum coherence.

In the main text, we argue that the interference contrast is a direct signature of the prepared state’s coherence. Here, we provide a rigorous quantitative validation of this claim. The total interference signal,  $P_g(\phi_1, \phi_2)$ , probes the state’s *total* coherence, which includes both the qubit-oscillator coherence and the coherence within the oscillator subspaces. It is given by

$$P_g(\phi_1, \phi_2) = P_g^{(1)} + P_g^{(2)} + P_g^{(3)} + c.c. \quad (\text{E14})$$

This signal can be decomposed via a Fourier series into components oscillating at different frequencies. As shown in Eqs. (D6-D8), the amplitudes of these Fourier components, denoted  $P_g^{(k)}$ , correspond directly to specific coherence terms (i.e., off-diagonal elements) in the state’s density matrix. For instance,  $P_g^{(1)}$  relates to coherences between Fock states differing by one quantum,  $P_g^{(3)}$  relates to coherences between states differing by three quanta, and so on.

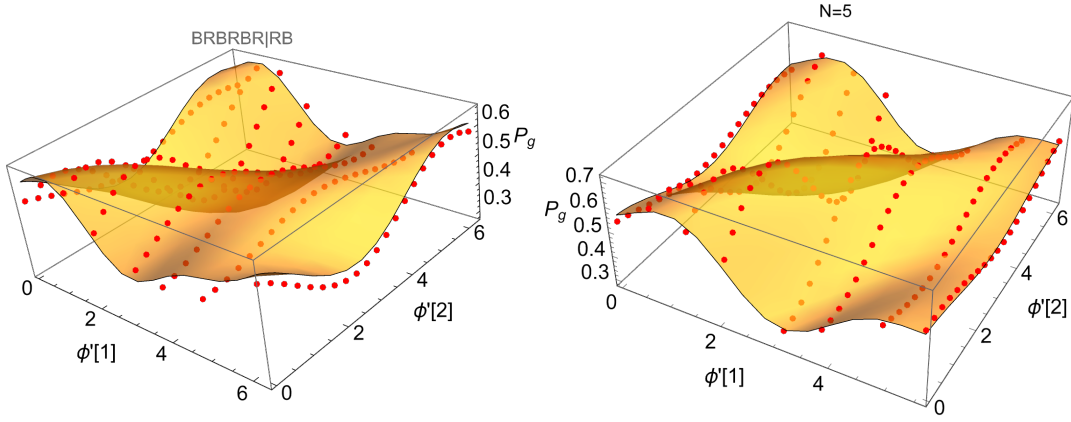


Figure F.1. Reconstruction of modulation for  $N = 6$  (BRBRBR|RB) and  $N = 10$ .

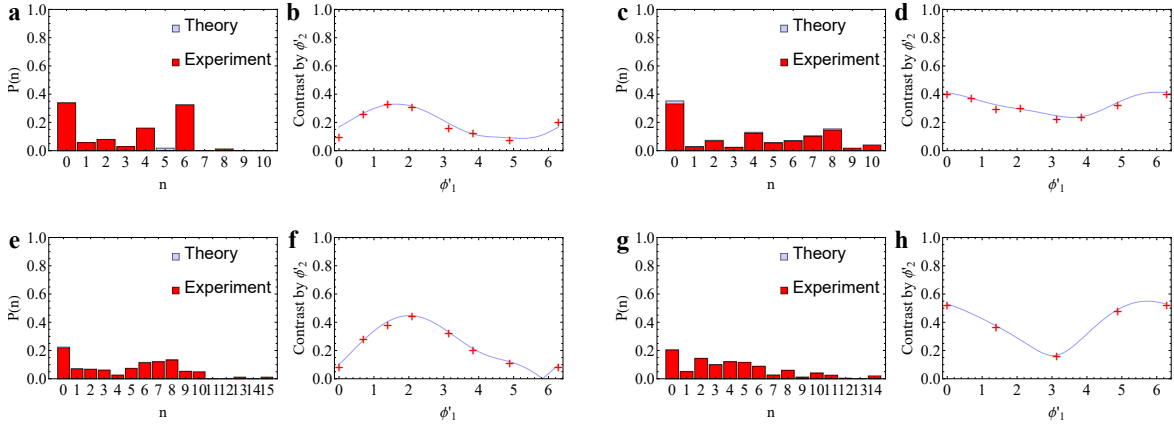


Figure F.2. Reconstruction of experimental phonon number distribution  $P(n)$  and the contrast by verification pulse phase for  $N = 6, 8, 10, 12$ .

The total contrast of the interference fringe, defined as the experimentally measured difference  $P_{\max} - P_{\min}$ , should therefore be determined by these individual coherence terms. To verify this, we checked the correspondence for a wide range of randomly sampled qubit-oscillator parity-entangled states, confirming the generality of this relationship beyond our specific preparation. The total contrast ("True Max") was found to be linearly dependent on the magnitudes of the first, second, and third-order coherence terms,  $R'(1) = |P_g^{(1)}|$ ,  $R(1) = |P_g^{(1)}|$ ,  $R(2) = |P_g^{(2)}|$  and  $R(3) = |P_g^{(3)}|$  ("Predicted Max"), specifically by the approximate formula

$$\approx 1.73R'(1) + 1.07R(1) + 1.14R(2) + 1.87R(2). \quad (\text{E15})$$

Figure E.1 plots this comparison across numerous experimental runs with different preparation sequences. The data points fall tightly along the line  $y = x$ , demonstrating a near-perfect linear relationship with a coefficient of determination  $R^2 \approx 0.94$ . Averaging over the preparation phases  $\varphi$  makes the correspondence of the coherence and average contrast very precise. This result serves as powerful, direct evidence for our central argument: the experimentally observed interference contrast is not merely related to coherence, but is quantitatively determined by the underlying quantum coherence pathways. This validates the use of contrast as a robust and accurate measure of the coherence present in the prepared state.

## Appendix F: Longer preparation sequence

Longer preparation sequences can be reconstructed similarly. In Fig. F.1 and F.2, we reconstructed modulation for  $N = 6$  that shows decoherence factor  $w = 0.535$  and  $N = 10$ , showing a good agreement.

### Appendix G: Contribution to $P_g$ by the off-diagonal elements in the prepared state

If the prepared state has the term  $|e, n\rangle\langle g, m|$  in the density matrix, it contributes to  $P_g$  after the verification pulses made of a red pulse as:

$$P_g[|e, n\rangle\langle g, m|] = i \sin[\kappa\sqrt{n+1}]z \cos[\kappa\sqrt{m}] \delta_{n-1, m}. \quad (\text{G1})$$

The only case that gives non-zero contribution is when  $n = m + 1$ . Terms with qubit states in  $|e\rangle\langle e|$  or  $|g\rangle\langle g|$  do not have terms with  $z$ , and thus is not modulating. If a verification blue pulse acts on the prepared state that has the term  $|e, n\rangle\langle g, m|$  in the density matrix, it contributes to  $P_g$  as

$$P_g = i \sin[\kappa\sqrt{n}] \cos[\kappa\sqrt{m+1}]z^* \delta_{n-1, m}. \quad (\text{G2})$$

The only non-zero term arises when  $n = m + 1$ . These results show that only the qubit coherence is contributing to the modulation of  $P_g$ .

While single pulses only probe first-order coherences ( $|n-m| = 1$ ), the combined RSB-BSB sequence acts as a multi-quantum operator. If the prepared state has the term  $|e, n\rangle\langle g, m|$  in the density matrix, it contributes to  $P_g$  after the verification pulses made of a red and a blue pulse given as:

$$P_g[|e, n\rangle\langle g, m|] = i \cos[\kappa\sqrt{n+1}] \sin[\kappa\sqrt{n}]z^* (\cos[\kappa\sqrt{m+1}] \cos[\kappa\sqrt{m}] \delta_{n-1, m} - \sin[\kappa\sqrt{m-1}]z \sin[\kappa\sqrt{m}]z^* \delta_{n-1, m-2}) \\ + i \sin[\kappa\sqrt{n+1}] \cos[\kappa\sqrt{n+2}]z (\cos[\kappa\sqrt{m+1}] \cos[\kappa\sqrt{m}] \delta_{n+1, m} - \sin[\kappa\sqrt{m-1}]z \sin[\kappa\sqrt{m}]z^* \delta_{n+1, m-2}) \quad (\text{G3})$$

where  $z = e^{i\theta}$ . This allows the sequence to bridge Fock states with higher separations, such as  $|n-m| = 3$ , through intermediate transitions. This term is the contribution of qubit coherence and oscillator coherence from terms that differ by odd quanta number, all containing the term  $Z = e^{i(n-m)\theta}$ . The two-pulse sequence functions as a multi-order filter. By expanding the product of the RSB and BSB unitaries, the resulting POVM contains terms proportional to  $|n\rangle\langle n \pm k|$ . For our specific pulse areas, the coefficients for  $k > 3$  vanish, isolating short-range coherence. Especially, the last term enables the interference by a terms that differ in quanta number by 3. From this, we can see that the maximum difference that can be read by such pulses is  $n - m = \pm 3$ .

If the prepared state has the term  $|e, n\rangle\langle e, m|$ , it contributes:

$$P_g[|e, n\rangle\langle e, m|] = i \cos[\kappa\sqrt{n+1}] \sin[\kappa\sqrt{n}]z^* (-i \cos[\kappa\sqrt{m+1}] \sin[\kappa\sqrt{m}]z \delta_{n-1, m-1} - i \sin[\kappa\sqrt{m+1}] \cos[\kappa\sqrt{m+1}]z^* \delta_{n-1, m+1}) \\ + i \sin[\kappa\sqrt{n+1}] \cos[\kappa\sqrt{n+2}]z (-i \cos[\kappa\sqrt{m+1}] \sin[\kappa\sqrt{m}]z \delta_{n+1, m-1} - i \sin[\kappa\sqrt{m+1}] \cos[\kappa\sqrt{m+2}]z^* \delta_{n+1, m+1}). \quad (\text{G4})$$

If the prepared state has the term  $|g, n\rangle\langle g, m|$ , it contributes:

$$P_g[|g, n\rangle\langle g, m|] = \cos[\kappa\sqrt{n+1}] \cos[\kappa\sqrt{n}] (\cos[\kappa\sqrt{m+1}] \cos[\kappa\sqrt{m}]z^* \delta_{n, m} - \sin[\kappa\sqrt{m-1}]z^* \sin[\kappa\sqrt{m+1}]z^* \delta_{n, m-2}) \\ + i \sin[\kappa\sqrt{n-1}] \sin[\kappa\sqrt{n}]z^* (\cos[\kappa\sqrt{m+1}] \cos[\kappa\sqrt{m}] \delta_{n-2, m} - \sin[\kappa\sqrt{m-1}]z^* \sin[\kappa\sqrt{m+1}]z^* \delta_{n-2, m-2}). \quad (\text{G5})$$

The two equations above capture the oscillator coherence, which cannot be measured by a single verification pulse. The verification pulse length  $\kappa$  can be chosen independently from the preparation pulse length  $t$ .

## Appendix H: Comparison to other methods

Our experiment can be compared to other methods using different qubit-oscillator interactions. For instance, a Rabi gate of the form  $\exp[it(e^{i\phi_R}\sigma_+\hat{a} + e^{-i\phi_R}\sigma_-\hat{a}^\dagger + e^{i\phi_B}\sigma_+\hat{a}^\dagger + e^{-i\phi_B}\sigma_-\hat{a})]$  can be synthesized digitally by rapidly alternating red and blue sideband pulses. Both gates suffer from phase

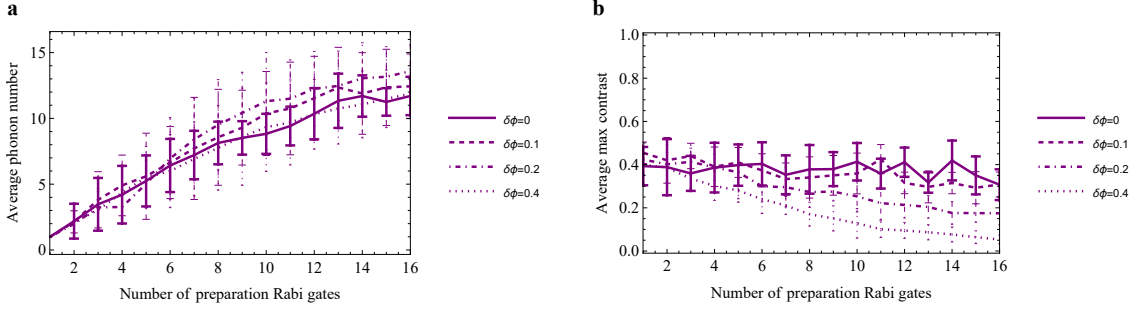


Figure H.1. Rabi gate analysis. **a** Average phonon number prepared via Rabi gates. It increases similarly as our experiment. **b** Maximum contrast by verification by Rabi gates. The maximum contrast decreases very rapidly by the phase instability in the preparation.

instability  $d\phi$ . These gates replace sideband pulses in preparation and verification. In Fig. H.1, this analysis with Rabi gates was investigated. With an increasing number of preparation Rabi pulses  $N$  and phase instability, the maximum contrast decreases. Sensitivity to phase instability also appears slightly greater than in our experiment, which is robust to phase instability up to  $\delta\phi \approx 0.8$ . This presents a different behavior compared to our experiment. The average phonon number increases analogously in both methods. When an arbitrary qubit-oscillator interaction is used for the verification, the contrast also declines sharply due to phase instability. Therefore, the large contrast under a phase instability is due to the nice property of the sideband verification method.

## Appendix I: Interferometric Fidelity and Visibility and Contrast

We first establish the general framework for quantifying interference, then explore the physical conditions that govern fringe visibility, and finally present numerical simulations demonstrating the robustness of high visibility against phase imperfections through practical optimization.

### 1. General Interferometric Framework

Interference phenomena in two-path systems, such as the qubit-oscillator states discussed, produce a measurement fidelity  $F$  that oscillates with a relative phase  $\phi$ . This dependence can be universally described by the form:

$$F(\phi) = a + b \cos(\phi) \quad (\text{I1})$$

The parameters  $a$  and  $b$  are determined by the overlaps of the prepared quantum states and the measurement involved. We use contrast and visibility to characterize the quality of the interference fringe: The contrast is defined as  $C = F_{\max} - F_{\min} = 2b$ . It measures the absolute probability swing and is directly related to the interference amplitude  $b$ . The visibility is given as  $V = (F_{\max} - F_{\min}) / (F_{\max} + F_{\min}) = b/a$ . A visibility of  $V = 1$  signifies that the fringe modulates perfectly from zero to its maximum, indicating perfectly balanced interfering pathways, even if the overall contrast is low.

### 2. Factors Governing Fringe Visibility

Our theoretical analysis reveals that fringe visibility is fundamentally tied to the balance between the two interfering quantum pathways. Any asymmetry in the magnitudes of the pathway amplitudes will degrade the visibility below its maximum value of 1.

a. *The Role of Pathway Balance*

We analyzed several simple conceptual models of general qubit-oscillator Schrödinger cat state  $\sqrt{w}|e\rangle|\alpha\rangle + e^{i\phi}\sqrt{1-w}|g\rangle|-\beta\rangle$ :

- **Balanced States:** For states of the form  $\frac{1}{\sqrt{2}}(|e\rangle|\alpha\rangle + e^{i\phi}|g\rangle|-\alpha\rangle)$ , the two interfering components have equal magnitude. This leads to  $a = b$  and thus a perfect visibility of  $V = 1$ , regardless of the coherent state amplitude  $\alpha$  or other phase mismatches. For example, if the prepared motional states are the coherent states  $|\psi_{\text{odd}}\rangle = |\alpha\rangle$  and  $|\psi_{\text{even}}\rangle = |-e^{i\theta}\alpha\rangle$ , where  $\theta$  is an unknown phase from the preparation interaction, the visibility remains unity irrespective of  $\theta$ . In the same example, the unnormalized contrast  $C$  would depend explicitly on the phase  $\theta$  and could be smaller than unity.
- **Amplitude Imbalance:** For a more general state with distinct coherent state components,  $|e\rangle|\alpha\rangle$  and  $|g\rangle|\beta\rangle$ , the visibility is degraded if the amplitudes differ, i.e.,  $|\alpha| \neq |\beta|$ . The interference is imperfect because the contributing state overlaps have unequal magnitudes.
- **Weight Imbalance:** If the qubit components themselves are unbalanced, as in  $\sqrt{w}|e\rangle|\alpha\rangle + e^{i\phi}\sqrt{1-w}|g\rangle|-\alpha\rangle$  with  $w \neq 1/2$ , the visibility is inherently reduced to  $V = 2\sqrt{w(1-w)} < 1$ . This is a direct consequence of the unequal probability amplitudes of the two “arms” of the interferometer.

b. *Restoring Visibility via Optimized Measurement*

Crucially, it is possible to counteract certain types of imbalance to regain the high visibility. Our analysis shows that even if an input state is prepared with unbalanced weights ( $w \neq 1/2$ ), perfect visibility ( $V = 1$ ) can, in principle, be restored by projecting onto a carefully chosen measurement state. Specifically, a measurement state with “swapped” weights ( $w' = 1 - w$ ) perfectly balances the interferometric pathways.

However, this restored visibility comes with a caveat: the absolute contrast remains limited by the initial imbalance. The maximum achievable contrast in this optimized scenario is  $C_{\text{opt}} = 4w(1-w)$ , which is always less than 1 for an unbalanced input. This highlights a key distinction: visibility speaks to the *balance* of interference, while contrast speaks to its absolute strength.

### 3. Numerical Simulation of Robustness to Phase Imperfections

To connect this theoretical understanding to more realistic experimental conditions, we performed numerical simulations of a preparation-detection sequence where pulse phases are stable but unknown (i.e., random for each sequence realization but fixed within it).

a. *Optimizing Pulse Areas without Phase Control*

Direct optimization of all pulse phases is experimentally demanding. We therefore investigated a more practical scheme where only the detection pulse *areas* (a proxy for strength and duration) are optimized to maximize interference, while the phases remain uncontrolled. The detection sequence length ( $N'$ ) was set equal to the preparation sequence length ( $N$ ).

b. *Simulation Results*

The simulations, summarized in Figure I.1, reveal a key finding:

- **High visibility can be maintained** across various circuit depths ( $N$ ) by optimizing only the detection pulse areas. This demonstrates that the system is robust against phase imperfections in its ability to produce clear, well-balanced interference fringes.
- **Average contrast remains low** and is highly sensitive to the lack of phase control.

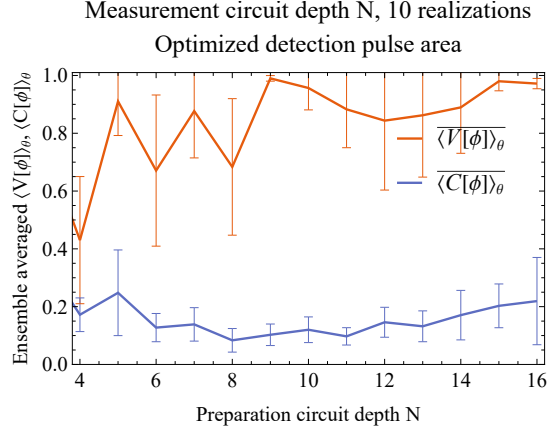


Figure I.1. Simulated average visibility  $\langle V \rangle$  and contrast  $\langle C \rangle$  versus preparation circuit depth  $N$ . The detection pulses depth were set as equal to  $N$ . For each realization, detection pulse areas were numerically optimized for a sequence with random preparation phases. The results show that high average visibility can be achieved, while average contrast remains low, demonstrating the robustness of visibility to phase imperfections.

#### 4. Conclusion

The combined theoretical and numerical results establish a clear hierarchy: fringe contrast is a fragile metric, sensitive to both state imbalances and phase errors. Fringe visibility, on the other hand, is a robust measure of the underlying coherence and optimality of the measurement. It is primarily sensitive to the balance of the interfering pathways, and our simulations show that high visibility can be maintained even in the absence of precise phase control by optimizing other accessible experimental parameters such as pulse area.

#### Appendix J: Experimental setup - Preparation and Measurement of Superposition States

The experimental verification of the presented scheme is carried out with a single  $^{40}\text{Ca}^+$  ion confined in a linear Paul trap with a RF frequency of 29.9 MHz and secular frequencies of  $\omega_{x,y,z} \sim 2\pi \times (2, 2, 1.1)$  MHz in the two radial and axial directions, respectively. The experimental sequence starts by initialization of the ion to  $|g, 0\rangle$  state by the combination of laser cooling and optical pumping pulses. Doppler cooling of all three normal modes is performed using a 397 nm laser red detuned from the  $4^2\text{S}_{1/2} \leftrightarrow 4^2\text{P}_{1/2}$  electric dipole transition by  $\approx 12$  MHz. The laser is directed at an angle  $\alpha \approx 45^\circ$  with respect to axial trap direction, within  $z-x$  plane. Simultaneously, the 866 nm laser beam, co-propagated along the same direction, is used for reshuffling the population of the  $3^2\text{D}_{3/2}$  manifold back to the cooling transition. A static magnetic field of  $|\vec{B}| = 3.3$  G is applied along the  $y$  axis. Both 397 nm and 866 nm laser beams are set to linear polarization oriented perpendicular to the magnetic field. Sideband cooling is applied on the quadrupole transition  $4^2\text{S}_{1/2}(m = -1/2) \leftrightarrow 3^2\text{D}_{5/2}, m = -5/2$  using a 729 nm laser. A regular sequence of short optical pumping pulses of  $\sigma$ -polarized 397 nm laser and a close-to-resonant 854 nm beam are set to reshuffle the electronic populations back to the  $4^2\text{S}_{1/2}(m = -1/2)$  level. Both the optical pumping 397 nm beam and the 854 nm repumper propagate along the axial direction. The resulting motional distribution corresponds to  $P_0 \approx 98\%$ .

As described in the main part of the article, the generation of large qubit-oscillator superposition states proceeds via  $N$ -times sequential iterative excitation of the blue (BSB) and red (RSB) sidebands on the  $|4^2\text{S}_{1/2}(m = -1/2)\rangle \leftrightarrow |3^2\text{D}_{5/2}(m = -5/2)\rangle$  transition. Each of these laser pulses is set to a constant pulse area given by the temporal length corresponding to  $\eta\Omega_0 t \approx \pi/4$ , where  $\eta$  is the Lamb-Dicke parameter,  $\Omega_0$  is the carrier Rabi frequency. The sequence begins with a resonant BSB, coherently exciting the electronic and motional states into a superposition of  $|0, g\rangle$  and  $|1, e\rangle$ . It is followed by successive RSB and BSB pulses, which produce the desired qubit-oscillator state described by Eq. (3) of the main article.

We investigate the resulting superposition state by three methods, schematically sketched in Fig. 1(c-e). First, we reconstruct the oscillator statistics, second, we analyze qubit-oscillator parity, and third,

we perform qubit-oscillator interferometry to analyze coherence of the produced state.

The reconstruction of the oscillator statistics proceeds by transferring the D-state population to the electronic ground state by applying a short pulse of 854 nm laser. Analysis of the time-resolved Rabi oscillations on the BSB transition then allows for motional population estimation by using the model

$$P_g(t) = \frac{1}{2} \left[ 1 + \sum_n P_n \cos(\Omega_{n,n\pm 1}t) \right] \exp^{-\gamma_n t} \quad (\text{J1})$$

where  $P_n$  is the occupation probability of the  $n^{\text{th}}$  motional state with estimated  $\Omega_0 = 2\pi \times 21.7 \pm 0.03$  kHz, and  $\gamma_n$  is decay rate which scales with mean phonon number as  $\gamma_n = \gamma_0(n+1)^{0.7}$  with  $\gamma_0$  varying from 0.06 to 0.13  $\text{ms}^{-1}$  depending on actual setup conditions. Here, we employed the parametrization of Rabi frequencies beyond the Lamb-Dicke approximation, i.e.  $\Omega_{n,n\pm 1} = \Omega_0 \left| \langle n \pm 1 | e^{i\eta(a+a^\dagger)} | n \rangle \right|$ , with  $\eta = 0.0629$ . The measurement of the  $P_g(t)$  is performed with the electron shelving method, realizing 100 repetitions of the experimental sequence to reduce the impact of the projection noise.

The analysis of qubit-oscillator parity follows a similar sequence, with the main distinction corresponding to the application of the 854 nm pulse prior to Rabi oscillation measurement and an additional post-selection on the electronic state. This enables reconstruction of the statistics of the odd and even oscillator parts independently. The post-selection is implemented again via electron shelving, that is, state-dependent fluorescence detection on the  $4^2\text{S}_{1/2} \leftrightarrow 4^2\text{P}_{1/2}$  transition. In the post-selection, we systematically retain and analyze only cases where the ion is found in the excited state  $|e\rangle$  as in this case, the oscillator statistics is unaffected by photon scattering. To access the ground state population, the post-selection is preceded by an additional carrier  $\pi$ -pulse, flipping the qubit population with minimal impact on the oscillator state. This is followed by measurement of Rabi oscillations on RSB and oscillator statistics reconstruction already described.

Both of these methods give us reliable results of the oscillator statistics, provided we choose sufficient sampling of the Rabi flops. To estimate the statistical uncertainty of the reconstruction we use a Monte-Carlo approach. The input statistical distributions are considered to correspond to the minimal uncertainty of each measured datapoint of  $P_g(t)$  given by the quantum projection noise described by the binomial distribution  $\sigma_{P_g} = \sqrt{\frac{P_g(1-P_g)}{N}}$ . The simulation of uncertainties of resulting parameters using this approach effectively captures the minimal statistical variation of our measurements. A least-squares method is used for the fit of the experimental data using Eq. J1, yielding an initial set of phonon populations. We implement and propagate  $N = 100$  random samples of each data point according to its binomial uncertainty.

To analyze the coherence of the prepared qubit-oscillator superposition states, we implement a Ramsey-type interference sequence corresponding to the single-pulse and two-pulse measurements described in the main text. The latter uses a sequence of an RSB pulse with the controllable phase  $\phi_1$  and BSB pulse with the controllable phase  $\phi_2$ . The first RSB pulse acts on  $|g, 2n+1\rangle \leftrightarrow |e, 2n\rangle$  transitions, probing qubit-oscillator coherence. The second BSB pulse address  $|e, 2n\rangle \leftrightarrow |g, 2n-1\rangle$ , enabling us to investigate the internal oscillator coherence. The method scans both phases  $\phi_1, \phi_2$ , leading to interference fringes shown in Figs. 4 and 5 in the main part of the manuscript. Interference by the single-pulse measurement method works equivalently but uses only the RSB pulse, thus accessing the complex qubit-oscillator coherence. The implementation of those methods in the experiment is as follows: After the preparation pulse sequence, a controllable time delay of  $\tau$  is set to test the decoherence of the prepared superposition states. After that, we apply interference by a single-pulse and two-pulse measurement scheme where we scan  $\phi_1$  or  $\phi_2$  to obtain an interference fringe pattern. Scanning only one of the phases is sufficient as the coherence test requires only sum or difference of  $\phi_1$  and  $\phi_2$ . This method allows us to probe the qubit-oscillator coherence and internal oscillator coherence even with the presence of an unknown but stable phase shift obtained during the pulse sequence preparation, inversion, and inserted time delay.

Apart from the fixed phase offsets of applied laser pulses, there is a dynamic phase drift caused by residual frequency difference  $\delta\omega$  between the oscillator frequency and the reference oscillator frequency. In addition, trap or laser frequency drifts, and magnetic field fluctuations, correspond to instabilities and decoherence, which are generally unavoidable but slow enough to observe the coherent phenomena on the demonstrated superpositions of up to  $\Delta n \approx 10$ . Those effects result in a phase evolution of the corresponding superposition state, which scales proportionally to the energy difference of the participating oscillator quanta. Spin coherence time estimated from the Ramsey interferometry by scanning the Ramsey time delay between two carrier  $\pi/2$  pulses corresponds to  $\sim 8$  ms, corresponding to 1/e time. It is primarily limited by laser phase noise and the long-term B-field drifts  $\sim 0.2$  mG/hr,

which, in addition, limit the overall duration of the measurements involving spin motional coherence of the Ramsey contrast but remain stable on the timescales of a few full pulse sequences. Motional coherence, estimated from the motional Ramsey interferometry for an equal superposition of  $|0\rangle$  and  $|1\rangle$ , defined by the exponential decay of the Ramsey fringe contrast, is  $\sim 100$  ms. It is predominantly attributed to motional heating, estimated  $\sim 3$  phonons/s and motional dephasing. The coherence decays faster for larger motional superpositions due to their increased sensitivity to drifts of the trapping frequency and faster diffusion of population for higher Fock states due to motional heating.

We note that the presented experimental tests of coherence were conducted over an overall time span of approximately one year, with the complete datasets corresponding to several weeks of continuous data acquisition. Such extended experimental time scales naturally introduce additional systematic variations in laboratory environmental conditions and include small improvements to the experimental apparatus. Consequently, minor discrepancies between different datasets may arise that are not fully captured by the statistically evaluated error bars presented here.

- 
- [1] W. H. Zurek, *Rev. Mod. Phys.* **75**, 715 (2003).
  - [2] K. Mølmer, *Phys. Rev. A* **55**, 3195 (1997).
  - [3] H. M. Wiseman, in *Fluctuations and Noise in Photonics and Quantum Optics*, Vol. 5111, edited by D. Abbott, J. H. Shapiro, and Y. Yamamoto, International Society for Optics and Photonics (SPIE, 2003) pp. 78 – 91.
  - [4] T. Rudolph and B. C. Sanders, *Phys. Rev. Lett.* **87**, 077903 (2001).
  - [5] S. J. Van Enk and C. A. Fuchs, *Phys. Rev. Lett.* **88**, 027902 (2002).
  - [6] A. D. Ludlow, M. M. Boyd, J. Ye, E. Peik, and P. O. Schmidt, *Rev. Mod. Phys.* **87**, 637 (2015).
  - [7] E. Schrödinger, *Naturwissenschaften* **23**, 807 (1935).
  - [8] S. Haroche and J.-M. Raimond, *Exploring the Quantum: Atoms, Cavities, and Photons* (Oxford University Press, Oxford, 2006).
  - [9] S. Omkar, Y. S. Teo, and H. Jeong, *Physical Review A* **111**, 053703 (2025).
  - [10] C. Monroe, D. M. Meekhof, B. E. King, and D. J. Wineland, *Science* **272**, 1131 (1996).
  - [11] M. Brune, E. Hagley, J. Dreyer, X. Maître, A. Maali, C. Wunderlich, J. M. Raimond, and S. Haroche, *Phys. Rev. Lett.* **77**, 4887 (1996).
  - [12] B. Vlastakis, G. Kirchmair, Z. Leghtas, S. E. Nigg, L. Frunzio, S. M. Girvin, M. Mirrahimi, M. H. Devoret, and R. J. Schoelkopf, *Science* **342**, 607 (2013).
  - [13] D. Leibfried, E. Knill, S. Seidelin, J. Britton, R. B. Blakestad, J. Chiaverini, D. B. Hume, W. M. Itano, J. D. Jost, C. Langer, R. Ozeri, R. Reichle, and D. J. Wineland, *Nature* **438**, 639 (2005).
  - [14] F. Fröwis, P. Sekatski, W. Dür, N. Gisin, and N. Sangouard, *Rev. Mod. Phys.* **90**, 025004 (2018).
  - [15] D. Gottesman, A. Kitaev, and J. Preskill, *Phys. Rev. A* **64**, 012310 (2001).
  - [16] J. Joo, W. J. Munro, and T. P. Spiller, *Phys. Rev. Lett.* **107**, 083601 (2011).
  - [17] K. C. McCormick, J. Keller, S. C. Burd, D. J. Wineland, A. C. Wilson, and D. Leibfried, *Quantum Science and Technology* **4**, 024007 (2019).
  - [18] Z. Leghtas, G. Kirchmair, B. Vlastakis, R. J. Schoelkopf, M. H. Devoret, and M. Mirrahimi, *Phys. Rev. Lett.* **111**, 120501 (2013).
  - [19] N. Ofek, A. Petrenko, R. Heeres, P. Reinhold, Z. Leghtas, B. Vlastakis, Y. Liu, K. Chou, L. Jiang, M. Mirrahimi, M. H. Devoret, and R. J. Schoelkopf, *Nature* **536**, 441 (2016).
  - [20] C. Flühmann, T. L. Nguyen, M. Marinelli, V. Negnevitsky, K. Mehta, and J. P. Home, *Nature* **566**, 513 (2019).
  - [21] C. Hempel, B. P. Lanyon, J. T. Barreiro, F. Huang, C. Senko, M. Cornelius, M. Olshanii, R. Blatt, C. F. Roos, and C. Monroe, *Nature Photonics* **7**, 630 (2013).
  - [22] D. Kienzler, H.-Y. Lo, B. Keitch, L. de Clercq, C. Flühmann, V. Negnevitsky, and J. P. Home, *Science* **347**, 53 (2015).
  - [23] S. Gerlich, S. Eibenberger, M. Tomandl, S. Nimmrichter, K. Hornberger, P. J. Fagan, J. Tüxen, M. Mayor, and M. Arndt, *Nature Communications* **2**, 263 (2011).
  - [24] P. T. Cochrane, G. J. Milburn, and W. J. Munro, *Phys. Rev. A* **59**, 2631 (1999).
  - [25] T. C. Ralph, A. Gilchrist, G. J. Milburn, W. J. Munro, and S. Glancy, *Phys. Rev. A* **68**, 042319 (2003).
  - [26] M. Mirrahimi, Z. Leghtas, V. V. Albert, S. Touzard, R. J. Schoelkopf, L. Jiang, and M. H. Devoret, *New Journal of Physics* **16**, 045014 (2014).
  - [27] M. H. Michael, M. Silveri, R. T. Brierley, V. V. Albert, J. Salmilehto, L. Jiang, and S. M. Girvin, *Phys. Rev. X* **6**, 031006 (2016).
  - [28] D. Leibfried, R. Blatt, C. Monroe, and D. Wineland, *Quantum dynamics of single trapped ions* (2003).
  - [29] C. H. Alderete, A. M. Green, N. H. Nguyen, Y. Zhu, B. M. Rodríguez-Lara, and N. M. Linke, *arXiv preprint arXiv:2108.05471* (2021).
  - [30] Z. L. Htoo, Z. Lasmar, C. H. Nguyen, K. W. Tseng, G. Maslennikov, D. N. Matsukevich, D. Kaszlikowski,

- and V. Scarani, *New Journal of Physics* **24**, 083002 (2022).
- [31] J. Hastrup, K. Park, J. B. Brask, R. Filip, and U. L. Andersen, *npj Quantum Information* **7**, 17 (2021).
  - [32] I. Yang, T. Agrenius, V. Usova, O. Romero-Isart, and G. Kirchmair, *Science Advances* **11**, 10.1126/sciadv.adr4492 (2025).
  - [33] A. Mezzacapo, U. L. Heras, J. S. Pedernales, L. DiCarlo, E. Solano, and L. Lamata, *Scientific Reports* **4**, 7482 (2014), turn JC and anti JC to Rabi.
  - [34] H.-P. Breuer, E.-M. Laine, J. Piilo, and H. M. Wiseman, *Physics Reports* **647**, 1 (2017).
  - [35] Q. A. Turchette, C. J. Myatt, B. E. King, C. A. Sackett, D. Kielpinski, W. M. Itano, C. Monroe, and D. J. Wineland, *Physical Review A* **62**, 053807 (2000).
  - [36] M. Brune, E. Hagley, J. Dreyer, X. Maître, A. Maali, C. Wunderlich, J. M. Raimond, and S. Haroche, *Phys. Rev. Lett.* **77**, 4887 (1996).
  - [37] B. Hacker, S. Welte, S. Daiss, A. Shaukat, S. Ritter, L. Li, and G. Rempe, *Nature Photonics* **13**, 110 (2019).
  - [38] O. Morin, K. Huang, J. Liu, H. Le Jeannic, C. Fabre, and J. Laurat, *Nature Photonics* **8**, 570 (2014).
  - [39] H. Jeong, A. Zavatta, M. Kang, S.-W. Lee, L. S. Costanzo, S. Grandi, T. C. Ralph, and M. Bellini, *Nature Photonics* **8**, 564 (2014).
  - [40] F. W. Knollmann, E. Clements, P. T. Callahan, M. Gehl, J. D. Hunker, T. Mahony, R. McConnell, R. Swint, C. Sorace-Agaskar, I. L. Chuang, J. Chiaverini, and D. Stick, *Optica Quantum* **2**, 230 (2024).
  - [41] D. Kienzler, H.-Y. Lo, B. Keitch, L. de Clercq, F. Leupold, V. Negnevitsky, and J. P. Home, *Phys. Rev. Lett.* **116**, 140402 (2016).
  - [42] W. T. Chen, J. N. Zhang, H. C. J. Gan, D. N. Matsukevich, and K. Kim, *Nature Physics* **19**, 1129 (2023).
  - [43] J. I. Cirac and P. Zoller, *Phys. Rev. Lett.* **74**, 4091 (1995).
  - [44] T. Monz, P. Schindler, J. T. Barreiro, M. Chwalla, D. Nigg, W. A. Coish, M. Harlander, W. Hänsel, M. Hennrich, and R. Blatt, *Phys. Rev. Lett.* **106**, 130506 (2011).
  - [45] M. Brownnutt, M. Kumph, P. Rabl, and R. Blatt, *Rev. Mod. Phys.* **87**, 1419 (2015).